Bioactive Materials 5 (2020) 1087–1101

Contents lists available at ScienceDirect

Bioactive Materials

journal homepage: http://www.keaipublishing.com/biomat

Electroactive barium titanate coated titanium scaffold improves osteogenesis and osseointegration with low-intensity pulsed ultrasound for large segmental bone defects

Bo Fan[a,b,1], Zheng Guo[a,*], Xiaokang Li[a,1], Songkai Li[b,1], Peng Gao[c,1], Xin Xiao[a], Jie Wu[a], Chao Shen[a], Yilai Jiao[d], Wentao Hou[d]

[a] Department of Orthopedics, Xijing Hospital, Fourth Military Medical University, Xi'an, 710032, China
[b] Orthopedic Centre-Spine Surgery, The 940 Hospital of Joint Logistics Support Force of Chinese People's Liberation Army, Lanzhou, 730050, China
[c] Department of Joint Surgery and Sports Medicine, Hunan Provincial People's Hospital and The First Affiliated Hospital of Hunan Normal University, Changsha, 410016, PR China
[d] Shenyang National Laboratory for Materials Science, Institute of Metal Research, Chinese Academy of Sciences, Shenyang, 110016, China

ARTICLE INFO

Keywords:
Large segmental bone defect
Barium titanate
Piezoelectric ceramic
Porous Ti6Al4V scaffold
Osteogenesis

ABSTRACT

For large segmental bone defects, porous titanium scaffolds have some advantages, however, they lack electrical activity which hinders their further use. In this study, a barium titanate ($BaTiO_3$) piezoelectric ceramic was used to modify the surface of a porous Ti6Al4V scaffold (pTi), which was characterized by scanning electron microscopy, energy dispersive spectroscopy, X-ray photoelectron spectroscopy, and roughness and water contact angle analyses. Low intensity pulsed ultrasound (LIPUS) was applied in vitro and in vivo study. The activity of bone marrow mesenchymal stem cells, including adhesion, proliferation, and gene expression, was significantly superior in the $BaTiO_3$/pTi, pTi + LIPUS, and $BaTiO_3$/pTi + LIPUS groups than in the pTi group. The activity was also higher in the $BaTiO_3$/pTi + LIPUS group than in the $BaTiO_3$/pTi and pTi + LIPUS groups. Additionally, micro-computed tomography, the mineral apposition rate, histomorphology, and the peak pull-out load showed that these scaffold conditions significantly enhanced osteogenesis and osseointegration 6 and 12 weeks after implantation in large segmental bone defects in the radius of rabbits compared with those resulting from the pTi condition. Consequently, the improved osteogenesis and osseointegration make the $BaTiO_3$/pTi + LIPUS a promising method to promote bone regeneration in large segmental bone defects for clinical application.

1. Introduction

In clinical practice, many bone defects are caused by bone trauma [1], infection [2], or tumors [3]. When the length of the bone defect exceeds a critical size (1.5 times the diameter of the tubular bone), it is defined as a large bone defect [4]. Clinical healing of large segmental bone defects is a challenging problem for the international orthopedic community because the bone's innate healing process is unable to complete bone regeneration at the deteriorated defect site. Supportive therapeutic intervention must also be provided. Therefore, methods using biomaterials [5] and tissue engineering [6] have been developed and utilized to support bone regeneration. However, due to a lack of essential vascularization and mechano-electric effects and poor biomechanical properties at the site of a large bone defect, the application of these methods is limited in clinical treatment. In this context, a comprehensive treatment strategy should be adopted. Furthermore, many requirements must be met, including a good material (biocompatible with adequate pore size and interconnectivity and stiffness similar to that of the surrounding tissue), a good coating (biocompatible with a mechano-electric effect), and even some other auxiliary measures.

For large segmental bone defects, porous titanium (Ti) alloy scaffolds can provide appropriate mechanical strength to maintain initial mechanical stability in load-bearing areas [7–10]. In addition, three-dimensional (3D) porous Ti scaffolds fabricated by electron beam melting (EBM) [11,12] show the advantages of appropriate pore size and adjustable interconnectivity. Thus, nutrients are more likely to diffuse into the center of scaffold, which is also good for new bone

Peer review under responsibility of KeAi Communications Co., Ltd.
* Corresponding author.
E-mail address: guozheng@fmmu.edu.cn (Z. Guo).
[1] These authors contributed equally to this work.

https://doi.org/10.1016/j.bioactmat.2020.07.001
Received 19 May 2020; Received in revised form 3 July 2020; Accepted 3 July 2020
2452-199X/ © 2020 The Authors. Publishing services by Elsevier B.V. on behalf of KeAi Communications Co., Ltd. This is an open access article under the CC BY-NC-ND license (http://creativecommons.org/licenses/BY-NC-ND/4.0/).

ingrowth [13,14]. Due to their lack of biological activity or mechano-electric effect, however, porous Ti scaffolds may fail to repair large bone defects.

Since entering the 21st century, the families of lead-free perovskite materials have received much attention in the last ten years because some significant progresses in their physical properties were realized [15]. All reported $BaTiO_3$-based ceramics based on tri-critical point (TCP)-type morphotropic phase boundary (MPB) show a rapid decrease of piezoelectricity away from the MPB, and their optimized d_{33} can be only achieved within a narrow composition/temperature region, resulting in poor property stability [16].

Recently, A new design strategy involving the multiphase convergence has been realized in (1–x) $Ba(Ti_{1-y}Sn_y)O_{3-x}$ $(Ba_{1-z}Ca_z)TiO_3$ ceramics, resulting in excellent overall properties with high piezoelectric coefficient and good temperature stability [17]. Barium titanate ($BaTiO_3$) piezoelectric ceramic is commonly employed to promote bone regeneration, which can mimic the stress-generated potentials (SGPs) of natural bone, which is itself a piezoelectric object [18], to produce micro-electric currents and promote calcium salt deposition at the bone defect site. When deformation of native bone occurs, it can generate piezoelectric polarization stimuli and adjust the growth of bone, shaping and rebuilding the tissue [19,20]. For piezoelectric ceramics, the piezoelectric effect can make them convert between mechanical energy and electrical energy, which is similar to the behavior of natural bone. Therefore, $BaTiO_3$ piezoelectric ceramic can be combined with porous Ti alloy scaffolds in the form of a coating by a wet chemical method to repair small bone defects. However, for large segmental defects, in the early stage of bone healing, the bone defect site cannot be weighted, which results in a local lack of mechanical stimulation. Eventually it will affect the function of piezoelectric ceramic coating and further affect the healing of bone tissue. Therefore, additional mechanical stimuli should be added.

Low-intensity pulsed ultrasound (LIPUS) as a mechanical wave can provide additional mechanical stimulation at the bone defect and act on the barium titanate coating, make it produce a piezoelectric effect, and promote bone regeneration. Meanwhile, Low-intensity pulsed ultrasound stimulation is a non-invasive physical therapy used to accelerate bone repair and promote bone healing. In 1994 and 2000, LIPUS was clinically approved for the treatment of fresh fracture and bone non-union, respectively, by the US Food and Drug Administration (FDA) [21,22]. Firstly, LIPUS can directly influence a series of cellular signal changes involved in the bone healing process, and therefore cause calcium ions to enter the cell and promote bone mineralization [23–25]. Secondly, LIPUS can increase the mRNA level of vascular endothelial growth factor A (VEGF-A), an important regulatory factor of angiogenesis. Lastly, LIPUS can stimulate cartilage cell proliferation, increase cartilage matrix production (type II collagen, glycosaminoglycan sugars, etc.), improve the maturity of newly formed bone, and ultimately promote the occurrence of endochondral ossification [26–28].

In this study, we deposited the $BaTiO_3$ composite as a piezoelectric coating onto the surface of porous Ti6Al4V scaffolds to form a composite Ti implant ($BaTiO_3$/pTi). The surface performance of the $BaTiO_3$/pTi implant was assessed by scanning electron microscopy (SEM), X-ray photoelectron spectroscopy (XPS), water contact angle measurement, and surface roughness analysis. Then, four groups were compared with each other, the pure titanium implant (pTi), the barium titanate/pure titanium implant ($BaTiO_3$/pTi), the pure titanium implant + low-intensity pulsed ultrasound (pTi + LIPUS), and the barium titanate/pure titanium implant + low-intensity pulsed ultrasound ($BaTiO_3$/pTi + LIPUS). The in vitro proliferation, apoptosis, and osteogenic differentiation of rabbit bone marrow mesenchymal stem cells (BMSCs) on the scaffolds were evaluated. The in vivo osteointegration and osteogenesis properties also were assessed using a large segmental defect model of the radius in New Zealand White rabbits.

2. Methods

2.1. Preparation of porous Ti alloy scaffolds

Medical grade Ti6Al4V powder was used to produce porous titanium (pTi) alloy scaffolds (porosity: 70–90%, average pore diameter: approximately 800 μm) by EBM technology. Briefly, the 3D structure of porous titanium alloy scaffolds was designed using CAD software. The structure was inputted into EBM devices (Arcam A1, Arcam AB, Mölndal, Sweden). Ti6Al4V powder was preheated to 650 °C with a 30 mA electron beam and 15,000 mm/s scanning speed and was then melted with a 6 mA electron beam and 400 mm/s scanning speed under vacuum (~10^{-4} to 10^{-5} mbar). When the processing of a plane was completed, a thin layer of fine metal powder was laid on the newly formed metal layer with a special device. The process was repeated until the whole porous Ti6Al4V scaffold had been prepared. Samples were fabricated into two shapes, cylinders and discs. Cylindrical samples (D: 5 mm, H: 13 mm) were used for animal experiments in vivo, and disk samples (D: 12 mm, H: 2 mm) were used for cell tests in vitro. All the experimental samples were in turn placed in acetone, ethyl alcohol, and deionized water, and an ultrasonic cleaning instrument was used to clean them for 10 min in each of the above solutions.

2.2. Preparation of $BaTiO_3$ piezoelectric ceramic coatings

Ti substrates were washed with twice distilled water and acetone in an ultrasonic cleaner. A mixture of 0.1 M barium hydroxide and 0.1 M potassium hydroxide in distilled water was poured into hydrothermal Teflon-lined autoclaves. Ti substrates were put into the above autoclaves. The autoclaves were then placed into a furnace at 180 °C for 8 h. After that, the Ti substrates were removed from the hydrothermal autoclaves, rinsed in distilled water, and dried.

2.3. Scaffold characteristics

2.3.1. SEM

Samples were fixed to the tray using conductive adhesive and sputtered with a thin layer of platinum (Pt) to enhance their conductivity. Then, they were placed into a field emission scanning electron microscope (FE-SEM, S-4800, Hitachi, Japan) to observe the samples' surface features. Meanwhile, EMAX ENERGY was used to perform energy dispersive spectroscopy (EDS) and to characterize the chemical and elemental composition of the samples.

2.3.2. XPS

The chemical composition of all the samples (pTi and $BaTiO_3$/pTi) was characterized by XPS using a Kratos Axis Ultra DLD spectrometer equipped with an Al Kαx-ray source (1486.6 eV, 5 mA × 15 kV). The XPS measurements were carried out at room temperature (RT) and 5×10^{-9} torr over an area of 700 × 300 μm on the sample surface. Six points were randomly selected on the surface of each sample, and three samples per condition were used for surface composition analysis. A flood gun delivered low-energy electrons to the samples during measurements to prevent charging effects on the polymeric surfaces. The software CasaXPS was used to analyze the acquired spectral data. After a Shirley background subtraction, each acquired spectrum could be broken up into individual mixed Gaussian-Lorentzian peaks. Then, the peaks of different chemical groups were added according to values found in literature.

2.3.3. Water contact angle and surface roughness

A contact angle goniometer (Dataphysics, Germany) was used to measure the surface water contact angle of the samples (pTi and $BaTiO_3$/pTi). Briefly, 5 μL of deionized water was dropped onto the sample surface. Then, the shape of the water drop was captured. The surface water contact angle was calculated using SCA20 software

(Dataphysics, Germany). To better investigate the difference in wettability, porous Ti6Al4V scaffolds were replaced with solid Ti6Al4V substrates. In addition, a confocal laser scanning microscope (Olympus, OLS4000, Japan) was used to analyze the surface roughness of the samples. Samples were placed on the platform, and an area of 1 × 1 mm was scanned to calculate the surface roughness of different samples. Six points were randomly selected on the surface of each sample, and six samples per condition were used for surface roughness analysis. Because these samples were porous, only the beams of the samples were scanned and calculated, and six points were also selected only on the beams.

2.3.4. Pore size、porosity and beam diameter

Micro-CT was used to scan the two scaffolds to assess the connectivity of them and the integrity of the beam of them. Meanwhile, the porosity and pore size of the two scaffolds were further measured to compare whether the basic structure and parameters of the scaffolds were affected before and after the preparation of the barium titanate coating. The scanning voltage of the Micro-CT system device was set to 80 KV, the scanning current was set to 500 μA, the rotation angle was set to 360°, and the scanning resolution was set to 13 μm. After the scaffolds are scanned, Micro-CT's own software was used to perform three-dimensional reconstruction of the obtained multi-layer scan data, and simultaneously to measure and analyze the structural parameters of the two scaffolds such as porosity, pore size and beam diameter.

2.3.5. The mechanical properties of the two scaffolds

The scaffolds were fixed to a hydraulics instrument (Instron 8872, Instron, USA). Then, the probe of the hydromechanical instrument gradually pressurized the scaffolds at a rate of 1 mm/min until their beam breaks. After testing, we could obtain the elastic modulus data and the axial compressive strength data of the two scaffolds.

2.4. In vitro cell studies

2.4.1. Isolation and culture of BMSCs

All institutional and national guidelines for the care and use of laboratory animals were followed. Primary BMSCs from a neonatal New Zealand White rabbit (age: 2 days) were isolated and cultured using the whole bone marrow adherent cell method. Briefly, the femur and tibia were extracted, and the marrow cavity was washed 2–3 times with complete medium (α-MEM medium supplemental with 10% fetal bovine serum, 100 U/mL penicillin, and 100 μg/mL streptomycin) using a 10 mL sterile syringe. Then, the bone marrow fluid was transferred into a Petri dish that was placed into an incubator at 37 ˚C with 5% CO_2 and 95% humidity. After 24 h and every 3 days thereafter, the culture medium was replaced with new medium. Upon reaching 80% confluence, the cells were passaged at a ratio of 1:3, and the cells in the third passage were seeded on the samples at a density of 1×10^{-5} cells/mL and randomized for incubation under the following conditions: (1) single porous Ti6Al4V scaffold (pTi); (2) porous Ti6Al4V scaffold covered with a $BaTiO_3$ piezoelectric ceramic coating ($BaTiO_3$/pTi); (3) porous Ti6Al4V scaffold treated with low-intensity pulsed ultrasound (pTi + LIPUS); (4) $BaTiO_3$/pTi treated with low-intensity pulsed ultrasound ($BaTiO_3$/pTi + LIPUS). A LIPUS exposure device (Sonicator 740, Mettler Electronics, USA) was used to perform the in vitro experiment. It was set to a 1.5 MHz sine wave with a pulse duration of 200 μs, a repeating pulse at 1 kHz, and an intensity of 30 mW/cm^2. The culture plate was then placed on the ultrasound transducer with a thin layer of water to maintain contact. LIPUS was applied through the bottom of the culture plates for 10 min daily at 37 ˚C for 4, 7, or 14 days.

2.4.2. Cell proliferation

When cells had been cultured on the samples under different conditions for 4 and 7 days, their proliferation was investigated using the cell counting kit-8 (CCK-8, Dojindo, Japan). In brief, at specified time points, each sample was removed from the old plate, washed twice with PBS, and placed in a new plate. Two milliliters of culture medium was poured into the new plate to drown the samples in each group. Then, the appropriate amount (about 0.2 mL) of CCK-8 reagent was also added to each sample in the plate. The new plate was then transferred to the incubator (37 ˚C, 5% CO_2, and 95% humidity) and kept there for 4 h. Finally, 100 μL of solution was obtained from the different samples and placed into a spectrophotometer to measure the optical density at 450 nm.

CCK-8 is a sensitive colorimetric assay that measures the number of viable cells to determine cell proliferation and cytotoxicity by utilizing WST-8 [2-(2-methoxy-4-nitropheny)-3-(4- nitropheny)-5-(2,4-disulfophenyl)-2H-tetrazolium, monosodium salt]. In the presence of an electron mediator, WST-8 is reduced by dehydrogenases in cells to give an orange-colored product (formazan), which is soluble in the tissue culture medium. The amount of the formazan dye generated by dehydrogenases in the cells is directly proportional to the number of living cells. The absorbance at 450 nm is measured using a microplate reader.

2.4.3. Cell adhesion and morphology

When cells had been seeded on the samples for 4 and 7 days, samples were fixed with 4% paraformaldehyde (PFA) in PBS for 15 min and permeabilized with 0.1% Triton-X 100 in PBS for 5 min. After being blocked with 1% bovine serum albumin (BSA) in PBS for 30 min, samples were incubated with a primary antibody against vinculin (1:200, Abcam) at 4 ˚C overnight. Subsequently, samples were washed with PBS three times and then incubated with a fluorescein isothiocyanate (FITC)-conjugated goat anti-rat secondary antibody (1:100) at RT for 1 h. After the vinculin staining process, samples were stained with rhodamine-phalloidin (Cytoskeleton, Inc.) for 30 min at RT for visualization of filamentous actin (F-actin), and nuclei were counterstained with 4′,6 diamidino-2-phenylindole (DAPI). Finally, an Olympus confocal laser scanning microscope was used to capture images. The vinculin expression and ratio of the overall cellular area to the nuclear area (CN ratio) were measured using Image-Pro Plus software.

After incubation for 4 days, samples were fixed in 2.5% v/v glutaraldehyde at 4 ˚C for 24 h. An ethanol gradient (30%, 50%, 70%, 90%, 100%) was used to dehydrate them, and each step was maintained for 15 min. After being freeze-dried, the samples were sputtered with Pt for SEM imaging. For each group, FE-SEM (S-4800, Hitachi, Japan) was used to examine cell morphology and analyze cell connections.

2.4.4. LIVE/DEAD cell fluorescent stain and apoptosis

When cells in the different groups had been cultured for 4 and 7 days, a LIVE/DEAD Cell Imaging kit (Thermo Fisher Scientific, USA) was used to visualize the live and dead cells. Briefly, to thaw the LIVE/DEAD Cell Imaging kit, it was first placed at RT for 5 min. Secondly, a Live Green vial was transferred into the Dead Red vial and fully mixed to create a 2 × stock. Thirdly, the 2 × stock was added to different groups with equal volume, followed by incubation for 15 min in the dark at RT. Lastly, the samples were washed twice with PBS and then observed under a fluorescent microscope. Live cells were marked as green with FITC (green fluorescent dye), and dead cells were marked as red with Texas Red (red fluorescent dye). The percentage of dead cells to total cells (DC/TC percentage) was calculated from six fields randomly selected under a microscope.

After the different groups were incubated for 4 days, the cell apoptosis rate was analyzed with Annexin V-FITC/propidium iodide (PI) double-staining using a flow cytometer (FACS Vantage SE, BD Biosciences). Briefly, cells were collected in each sample and re-suspended with complete medium at 1×10^6 cells/mL. Meanwhile, Annexin V-FITC (50 μL) was added into the cell suspension (1 mL) and the samples were incubated for 10 min in the dark at RT. Then, binding buffer (1.5 mL) and PI (15 μL) were added, and all the samples were

immediately measured with the flow cytometer.

2.4.5. Detection of alkaline phosphatase (ALP) activity and analysis by real-time quantitative PCR (RT-PCR)

Osteogenic medium was prepared by adding dexamethasone (10 mg/mL), beta glycerin sodium phosphate (10 μg/mL), and ascorbic acid-C (50 μg/mL) to complete medium. Then, the samples seeded with cells were transferred into the osteogenic medium and incubated for 7 and 14 days. The medium was replaced every 3 days.

The alkaline phosphatase (ALP) activity of each sample was measured at each time point using *p*-nitrophenyl phosphate (pNPP) (Sigma, Ventura, USA) and a spectrophotometric plate reader at 405 nm. The total protein concentration was determined using a micro-BCA assay kit. The ALP activity was finally normalized to the total protein concentration correspondingly and expressed as μmol/h/mg protein.

Cells cultured under different conditions were collected to evaluate their differentiation by determining the expressions of the genes for ALP, osteopontin (OPN), runt-related transcription factor-2 (Runx2), and collagen type 1 (Col-1). Briefly, the total RNA was extracted according to the instructions for the RNA extraction kit (TRIzol reagent, Invitrogen, Life Technologies). The obtained RNA was used to form cDNA by reverse transcription using PrimeScript RT Master Mix (Takara), and the Bio-Rad CFX96 PCR Manager system was used to perform real-time PCR. The primers used in this study are listed in Table 1. GAPDH was used as a housekeeping gene.

2.5. In vivo animal studies

2.5.1. Surgical procedures

Ninety-six healthy New Zealand White rabbits aged 8–10 months and weighing 2.5–3.5 kg (2.91 kg on average) were used for the in vivo animal experiments. The middle part of the radius of all rabbits was replaced with $BaTiO_3$/pTi or pTi samples, and the animals were randomly separated into the following four groups: (1) pTi; (2) $BaTiO_3$/pTi; (3) pTi + LIPUS; and (4) $BaTiO_3$/pTi + LIPUS. Each group was further divided into two subgroups with implant durations of 6 and 12 weeks.

Pentobarbital (3%, 1 mL/kg) and xylazine hydrochloride (0.1 mL/kg) were used to anesthetize these animals by intramuscular injection. The rabbits' forelegs were shaved, and then the animals were fixed on an operating table in the lateral position. After the surgical area was disinfected with iodine and covered with a sterile drape, the radius was exposed via a 3 to 4 cm-long incision. The middle part of the radius was removed to establish a bone defect model (length: 13 mm). To completely remove skeletal scraps, the defect was washed twice with hydrogen peroxide and normal saline. Afterward, $BaTiO_3$/pTi or pTi samples were implanted into the defects, the incisions were closed layer by layer with silk sutures, and the surgical area was sterilized again with iodine. To prevent wound infection, gentamycin sulfate (40,000 U/d) was routinely administered intramuscularly once a day for 3 days after the surgery. After surgery, the LIPUS exposure device was immediately used on the pTi + LIPUS and $BaTiO_3$/pTi + LIPUS groups with the same parameters as described previously in the cell studies. In brief, the ultrasound transducer was placed on the skin of the forelegs with a thin layer of coupling agent to maintain contact. LIPUS was applied through the skin of the forelegs for 20 min daily for 6 or 12 weeks. At those time points, the rabbits were sacrificed by injecting 20 mL of air into the marginal vein, and the specimens containing the implants were obtained and placed in 80% ethanol for further examination.

Table 1
Primers used in real-time PCR.

Gene	Forward primer sequence (5′- 3′)	Reverse primer sequence (5′- 3′)
ALP	TGACGTGATCATGGGTGGC	CCAGACAAAGTGGGAGTGCT
OPN	TAAACACGCTGATTCGGGC	CTTTCAATGGACTTACTCGGGA
Runx2	GTGGAGCTGCGGACGATGAA	AGATCAGTTGGCATCCGGG
Col-1	AGGAGAGAAAGGAACCAAGGGAC	AGCACCAGGGAAACCAGTCATA
GAPDH	ACCACGGTGCACGCCATCAC	TCCACCACCCTGTTGCTGTA

2.5.2. Qualitative micro-computed tomography (micro-CT) assessment

After the specimens were harvested, the new bone and implants were analyzed using a micro-computed tomography (micro-CT) imaging system (Y.Cheetah, YXLON, Germany). Briefly, specimens were placed in the sample holder and scanned under the following conditions: scan resolution, approximately 13 μm; scanning angular rotation, 360°; source voltage, 80 kV; and beam current, 500 μA. Two-dimensional images were obtained by the FGUI 3.0 operating software, and 3D images were obtained by the operating software VG Studio 2.1. Meanwhile, the area of the implant (D: 5 mm, H: 13 mm) was marked as the region of interest (ROI). To decrease metal artifacts, beam hardening correction was performed. The threshold for new bone was set to 300–1300, and the threshold for implants was set to 1300–4000. Then, 3D images of the ROI were reconstructed to evaluate the 3D microarchitecture. Finally, the ratio of bone volume to the total volume (BV/TV) in the ROI was calculated.

2.5.3. Fluorescent labeling of newly formed bone

To detect the new bone growth rate, tetracycline and calcein were used to mark new bone tissue at 6 and 12 weeks. In brief, tetracycline was dissolved in physiological saline at 50 mg/mL. Thirteen days before the rabbits were sacrificed, they began to be injected intramuscularly with the tetracycline solution (50 mg/kg) once a day for 3 days. Ten days after that, a calcein solution was prepared (calcein: 0.5 g, sodium bicarbonate: 2 g, physiological saline: 100 mL) and injected (8 mg/kg) the same way as the tetracycline solution. After the specimens were fixed in 80% ethanol for 3 days, they were dehydrated step-by-step in the following solutions: ethanol (70%, 80%, 90%), normal butanol, absolute ethyl alcohol, and xylene. Then, they were embedded in poly (methyl methacrylate) (PMMA) resins that polymerized and coagulated at 50 °C within 3 days. Afterward, a modified interlocked diamond saw (Leica Microtome, Wetzlar, Germany) was used to cut the embedded specimens into thin sections (approximately 150 μm in thickness), and a hard tissue slice-lapping machine was used to micro-grind these sections until their thickness was about 40 μm. Finally, the yellow fluorescence (tetracycline) and green fluorescence (calcein) in the new bone were excited under blue light using a standard optical microscope (Leica LA Microsystems, Bensheim, Germany). Fluorescence images were collected using Viewfinder Version 3.0.1 software (Pixera, USA), and the bone mineral apposition rate (MAR) was calculated using Image-Pro Plus software (Media Cyberbetics, USA).

2.5.4. Histological and histomorphometric analysis

After fluorescence images were collected, all sections were stained with 1.2% trinitrophenol and 1% acid fuchsin (Von-Gieson staining) to be used for histological analysis. Briefly, these sections were put into 0.1% formic acid solution for 3 min and washed with running water for 3 min. Then, they were transferred into a 20% methanol solution to soak for 3 min. After being washed by running water for 3 min, they were put into Stevenel's Blue dye liquor at 60 °C for 3 min and rinsed with 60 °C distilled water for 3 min. After that, they were stained with trinitrophenol-acid fuchsin distilled water for 15 min at RT. They were transferred into absolute ethyl alcohol for 10 s to remove excess dye solution from the sections, and dry filter paper was used to remove residual alcohol. Finally, a standard optical microscope equipped with Viewfinder Version 3.0.1 software was used to collect histological images. The qualitative analysis of newly formed bone was measured with Image-Pro Plus software. Based on the Von-Gieson staining, the bone volume percent (the ratio of the newly formed bone tissue area to the implant area) was calculated.

2.5.5. Biomechanical testing

Biomechanical studies were performed on six experimental specimens in each group at 6 and 12 weeks. After the middle part of the radius, including the implant (length: about 3.3 cm), was acquired, the muscles, ligaments, and fibrous tissue were thoroughly removed around the implant and bone. Some bone tissue (length: 1 cm on the vertical axis) was left at opposite ends of the specimens. A soft iron wire (diameter: 1 mm) was used to wrap the middle (on the long axis) of the implant through the gap between the implant and the ulna. Because the shape of the acquired specimens was irregular and could not be clamped with mechanical testing equipment, they needed to be embedded in poly (methylmethacrylate) for rigid fixation on the mechanical testing equipment. Briefly, resin powder and self-solidification resin liquid were mixed at a weight ratio of 2:1 and transferred into a copper mold (cuboid, length: 3.5 cm, width: 1.5 cm, and height: 2 cm). When the mixture became a doughy plastic material, the ulna and radius of the specimen were encased in the mixture. The implant and soft iron wire were not embedded in poly (methylmethacrylate). Then, a tension test was performed with a CMT4304 testing apparatus (MTS, US), and the peak pull-out load (N) of the implants ($n = 6$) was calculated. A constant increase in the tensile speed of 1 mm/min was applied to the specimens with 0 N preload. The test was not stopped until the implant and the bone tissue around it were completely separated.

2.6. Statistical analysis

All of the data were statistically analyzed with the SPSS 17.0 software package (SPSS Inc., Chicago, USA) and presented as the mean ± SD for each group. At each time point, the different conditions were compared using a one-way ANOVA, and further multiple comparisons were made using the least significant difference (LSD) method. Comparisons between two different time points (i.e., 6 and 12 weeks postoperatively) for the same condition were performed using t-tests. $p < 0.05$ was considered statistically significant.

3. Results

3.1. Scaffold characterization

3.1.1. SEM and EDS analysis

Through a series of modifications, we observed that the color of pTi modified with $BaTiO_3$ was blue to the naked eye (Fig. 1 B1 and B2) and that the color of pTi was gray (Fig. 1 A1 and A2). Moreover, SEM and EDS showed that $BaTiO_3$ (Fig. 1 B5 and D) was successfully immobilized on the surface of pTi. No change in the surface morphology was clearly observed between pTi and $BaTiO_3$/pTi at low magnification (Fig. 1 A3, A4, B3, and B4), but the change was obvious at high magnification (Fig. 1 A5 and B5). Furthermore, there were many small folds and granular protuberances on the surface of $BaTiO_3$/pTi at 10,000 × magnification, while the surface of pTi was smooth and flat. The EDS data (Fig. 1C and D) further showed that the $BaTiO_3$ coating was successfully immobilized on the surface of the pTi scaffold because barium was observed in the EDS data (Fig. 1 D).

3.1.2. XPS analysis

Superficial elements and the chemical composition of the surface of the implants (pTi and $BaTiO_3$/pTi) were analyzed by XPS. As shown in Fig. 2 A3 and A4, we observed from the element spectrum diagram that there were a number of elemental peaks that differed between the pTi and $BaTiO_3$/pTi implants. In addition, the barium element bands of the elemental spectrum diagrams for the two implants were analyzed. No barium peak was found on the pTi implant (Fig. 2 B3), while it was obviously observed on the $BaTiO_3$/pTi implant (Fig. 2 B4). These results indicated that the $BaTiO_3$ coating successfully modified the surface of the porous Ti6Al4V scaffolds.

3.1.3. Water contact angle and surface roughness

The average water contact angle of the Ti6Al4V scaffolds with a $BaTiO_3$ coating was 40.22° ± 1.38°, while that of the bare Ti6Al4V scaffolds without a $BaTiO_3$ coating was 77.28° ± 3.47°. These results had statistical significance, indicating that $BaTiO_3$/pTi was significantly more hydrophilic than pTi. That is, the $BaTiO_3$ coating successfully enhanced the wettability of pTi (Fig. 2 A1, B1, and C). Thus, compared with pTi, the $BaTiO_3$ coating was more conducive to cell adhesion. In addition, the $BaTiO_3$ coating significantly improved the surface roughness (Fig. 2 A2, B2, and D), as the data showed that the average surface roughness of $BaTiO_3$/pTi was 5.78 ± 1.36 μm while that of pTi was 8.69 ± 1.22 μm. These results imply that $BaTiO_3$/pTi had a larger specific surface area than pTi and provided more area for cell adhesion.

3.1.4. Pore size、porosity and beam diameter

Through Micro-CT testing, the integrity and connectivity of all the beams of the two brackets were good, and no obvious fractures of the

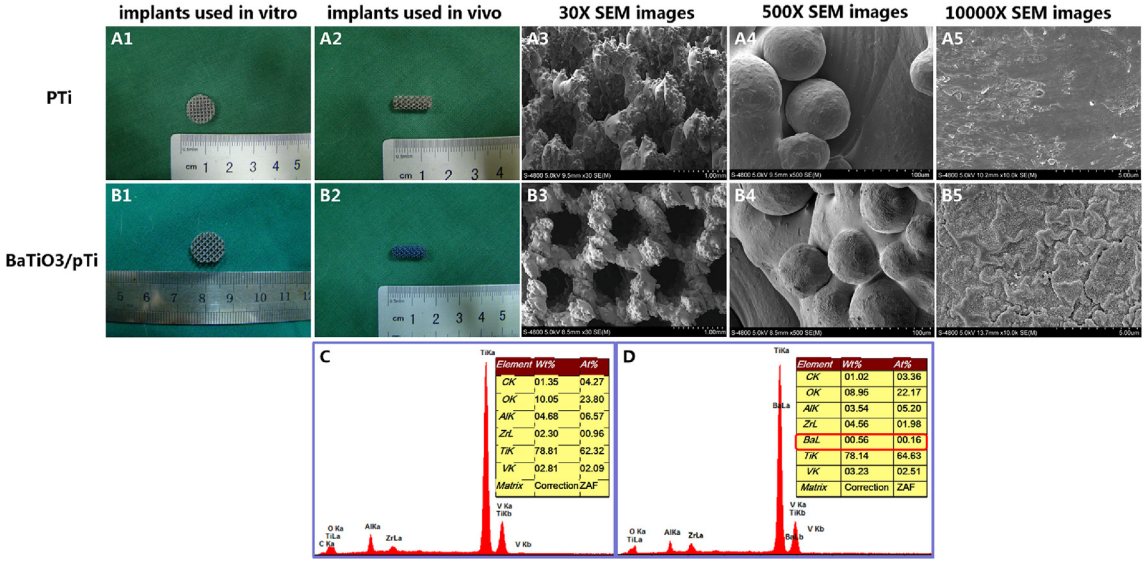

Fig. 1. Gross view and SEM images of surface morphology of porous Ti6Al4V scafflod (pTi, A1–A5) and barium titanate coated porous Ti6Al4V scafflod (BaTiO3/pTi, B1–B5). EDS data for pTi (C), BaTiO3/pTi (D). The presence of barium element in the EDS indicated that BaTiO3 was successfully immobilized on the scaffolds (D).

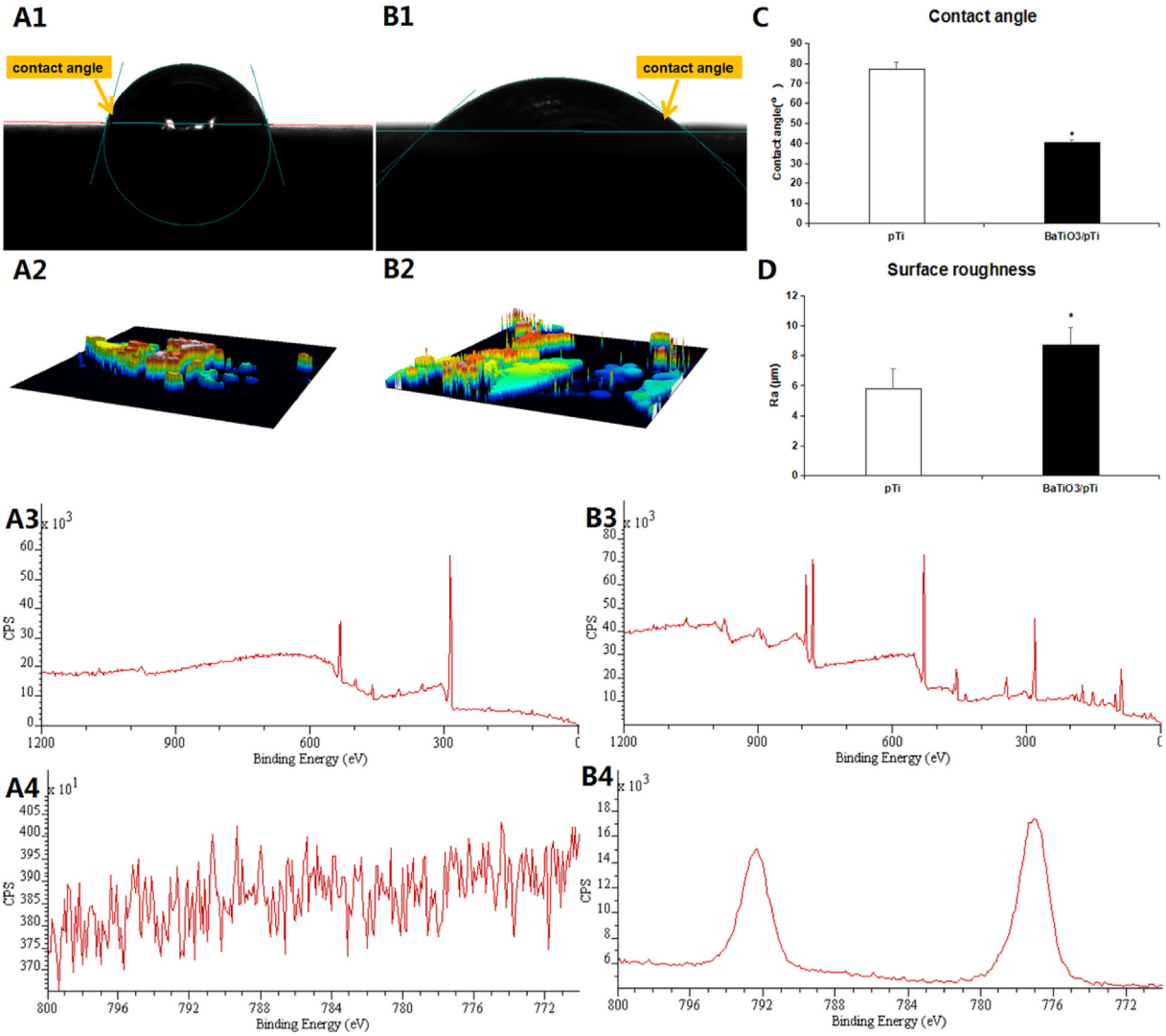

Fig. 2. Water contact angle measurement for the Ti6Al4V substrate (A1) and Ti6Al4V substrate with $BaTiO_3$ coating (B1). Average water contact angle analysis (C). Surface CLSM images of the Ti6Al4V substrate (A2) and Ti6Al4V substrate with $BaTiO_3$ coating (B2). Surface roughness analysis (D). Elements distribution diagram of XPS for the Ti6Al4V substrate (A3, A4) and Ti6Al4V substrate with $BaTiO_3$ coating (B3, B4). Asterisks (*) indicate statistical significance, $p < 0.05$.

inner and outer beams were found. The pore size of pTi scaffold was 663 ± 42 μm, the porosity was 70% ± 5.3%, and the beam diameter was 382 ± 23 μm. The pore size of $BaTiO_3$/pTi scaffold was 659 ± 52 μm, the porosity was 71% ± 8.9%, and the beam diameter was 383 ± 14 μm. After statistical analysis, the parameters (pore size、porosity and beam diameter) of the two scaffolds were not significantly different. This shows that the barium titanate coating will not significantly affect the basic structure and parameters of the porous Ti6Al4V scaffolds(Fig. 3).

3.1.5. Elastic modulus and compressive strength of the two scaffolds

The elastic modulus of pTi was 2.6 ± 0.1 Gpa, and the compressive strength was 65 ± 4 Mpa. The elastic modulus of $BaTiO_3$/pTi was 2.8 ± 0.3 Gpa, and the compressive strength was 63 ± 6 Mpa. The elastic modulus and compressive strength of the two stents were not statistically different(Fig. 4).

3.2. In vitro testing

3.2.1. Cell viability

After 4 and 7 days of culture, the proliferation of cells in each group was tested using the CCK-8 assay to assess cellular activity. Cell viability was found to increase with increased incubation time in the pTi, $BaTiO_3$/pTi, pTi + LIPUS, and $BaTiO_3$/pTi + LIPUS groups (Fig. 6 B). At 4 days, the cell viability was significantly higher in the $BaTiO_3$/pTi, pTi + LIPUS, and $BaTiO_3$/pTi + LIPUS groups than in the pTi group. The cell viability in the $BaTiO_3$/pTi + LIPUS group was also much greater than that in the $BaTiO_3$/pTi and pTi + LIPUS groups. Although the cell viability was higher in the pTi + LIPUS group than in the $BaTiO_3$/pTi group, no statistical difference was found in the cell proliferation between the two groups. After incubation for 7 days, the result was similar to that seen at 4 days. These data, therefore, suggest that $BaTiO_3$ promoted cell proliferation on the porous Ti6Al4V scaffolds, that LIPUS also promoted cell proliferation on the porous Ti6Al4V scaffolds, and that the combination of the two had a better effect on cell viability than each one had individually.

3.2.2. Cell adhesion and morphology

To analyze the cell adhesion state and cytoskeletal organization, BMSCs were fluorescently stained to mark F-actin (rhodamine-phalloidin), vinculin (FITC), and the nuclei (DAPI). As seen in Fig. 5, we observed that the cells spread out fully on the scaffolds in the $BaTiO_3$/pTi + LIPUS group and that their morphology was better than that in the other three groups. Although the actin bundles had a twisted

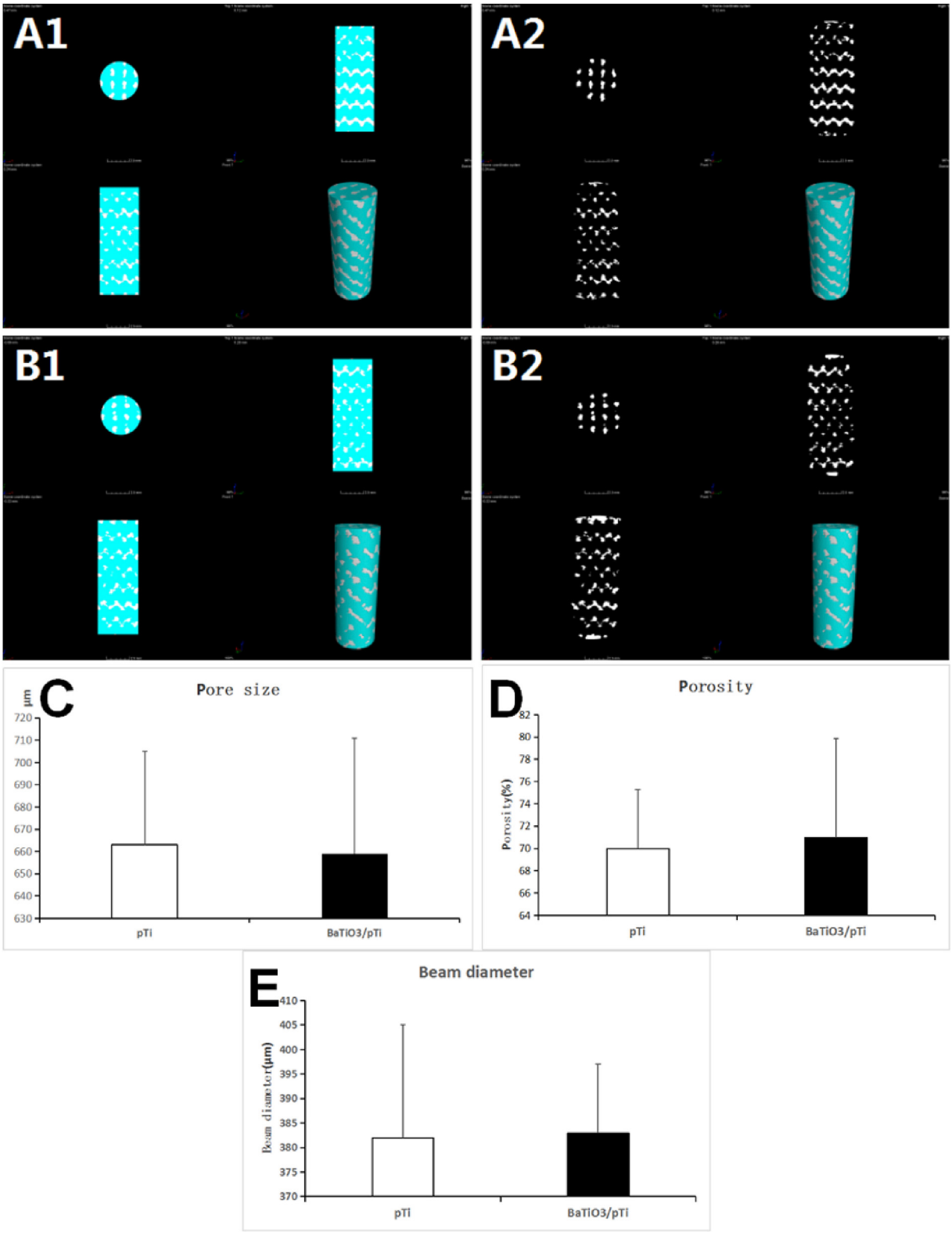

Fig. 3. Micro-CT scan results of two scaffolds. A is a Micro-CT image of $BaTiO_3$/pTi. B is a Micro-CT image of pTi. The light blue part in the picture is the porous structure of the scaffolds, and the white irregular bars are the metal trabecular structure of the scaffolds. A1, A2 and B1, B2 are the different representations of the two scaffolds' Micro-CT images. C is a statistical graph of the pore size of the two scaffolds. D is a statistical graph of the porosity of the two scaffolds. E is a statistical graph of the beam diameter of the two scaffolds. There was no statistically significant difference in pore size, porosity and beam diameter between the two scaffolds.

orientation in the $BaTiO_3$/pTi and pTi + LIPUS groups, the cell adhesion state was superior to that in the pTi group. Additionally, vinculin (green) was uniformly distributed in the cytoplasm and the cell borders in the $BaTiO_3$/pTi + LIPUS group, while it was mainly observed in the area around the nuclei in the other three groups. To the naked eye, the expression of vinculin in the $BaTiO_3$/pTi and pTi + LIPUS groups was higher than that in the pTi group. At 4 days, statistical analysis showed that cells in the $BaTiO_3$/pTi + LIPUS group had significantly higher CN

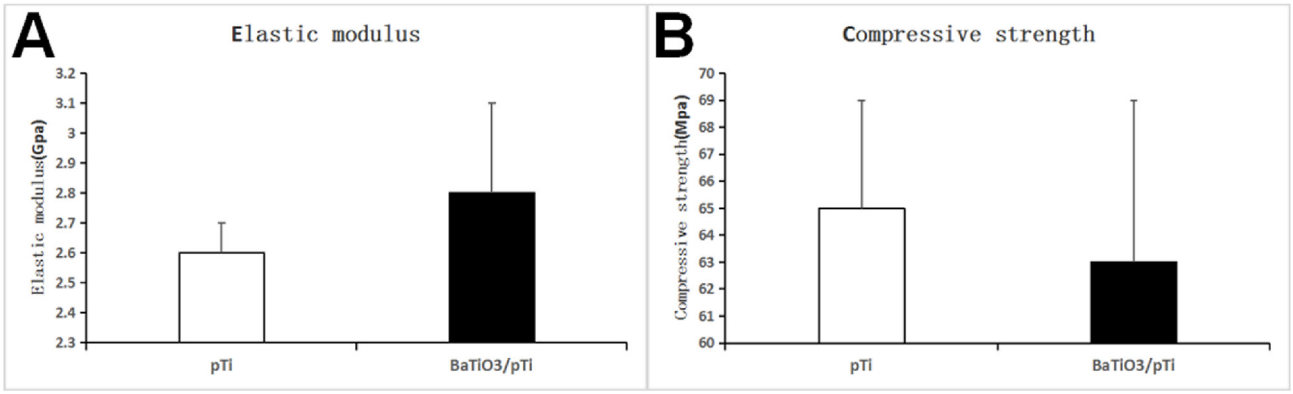

Fig. 4. A is a statistical analysis chart of the elastic modulus of the two scaffolds. B is a statistical analysis chart of the compressive strength of the two scaffolds. The elastic modulus and compressive strength of the two scaffolds were not statistically different.

ratios and vinculin fluorescence intensity than cells in the other three groups, that cells in the pTi + LIPUS group had higher CN ratios than those in the $BaTiO_3$/pTi and pTi groups, that there was no statistical significance in the CN ratios between the $BaTiO_3$/pTi and pTi groups, and that there was no significant difference in the vinculin fluorescence intensity among the three groups (pTi + LIPUS, $BaTiO_3$/pTi, and pTi). At 7 days, statistical analysis of the CN ratio and vinculin fluorescence intensity further indicated that these parameters were significantly higher in the $BaTiO_3$/pTi + LIPUS group than in the other three groups, that they were higher in the pTi + LIPUS and $BaTiO_3$/pTi groups than in the pTi group, and that there was no statistical difference between the pTi + LIPUS and $BaTiO_3$/pTi groups.

SEM images of the cellular morphology under different conditions were captured after 4 days of incubation (Fig. 6 A). In the pTi group, the BMSCs had extending pseudopodia but exhibited a widely spread and flattened shape. They were sparsely distributed and appeared atrophied on the scaffolds. By contrast, in the $BaTiO_3$/pTi, pTi + LIPUS, and $BaTiO_3$/pTi + LIPUS groups, the BMSCs had good appearance and high density, and cytoplasmic extrusions could be observed. However, the cell stretch was lower in the $BaTiO_3$/pTi and pTi + LIPUS groups than in the $BaTiO_3$/pTi + LIPUS group. Furthermore, the BMSCs overlapped with each other to form a cell layer that mostly covered the varying surface in the $BaTiO_3$/pTi + LIPUS group. At the same time, cellular filopodia anchored cells to the surface of the $BaTiO_3$ coating substrate, and it is worth noting that cellular junctions were established, although they were not easy to find. In short, the $BaTiO_3$/pTi + LIPUS-cultured cells had better morphology and were present in higher quantity. Thus, these results suggest that the $BaTiO_3$ coating and LIPUS improved cell adhesion and morphology, respectively, and that the combination of the two played a larger role than each on its own.

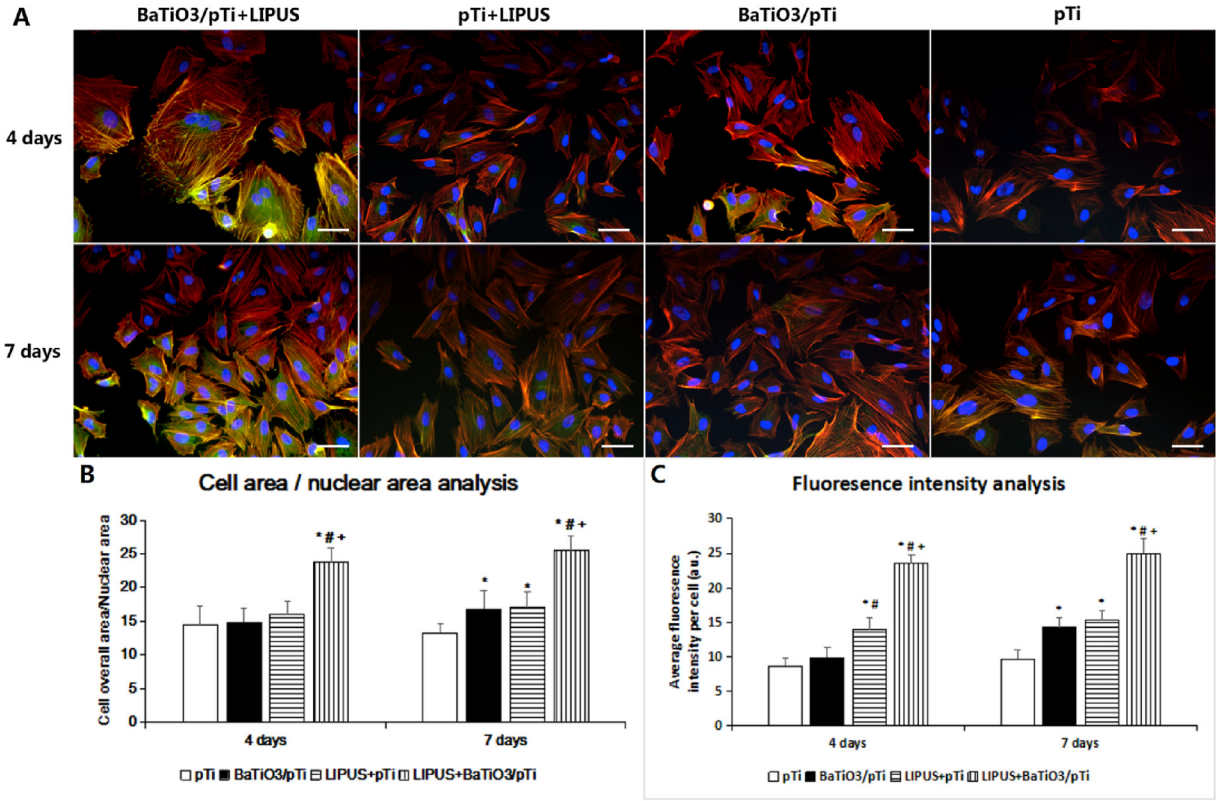

Fig. 5. (A) Fluorescent staining of BMSC cells in different groups (red, Rhodamine-phalloidin for F-actin; blue, DAPI for nucleus; green, fluorescein isothiocyanate for vinculin.) and (B) analysis of morphology and (C)fluorescence intensity of vinculin staining for cells on different scaffolds. *p < 0.05 vs. pTi, #p < 0.05 vs. $BaTiO_3$/pTi, +p < 0.05 vs. pTi + LIPUS. Scale bar: 50 μm.

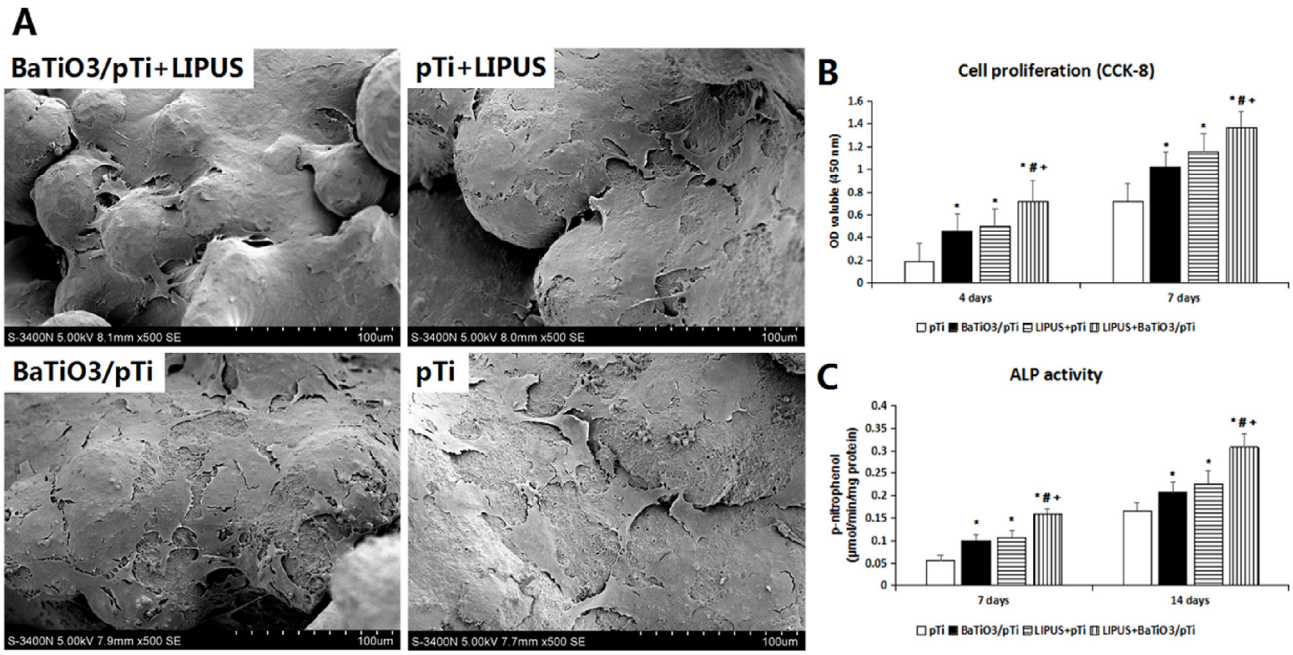

Fig. 6. SEM images of BMSCs morphology in different groups after incubation for 4 days.

3.2.3. Analysis of live/dead cells and cell apoptosis

Live/dead cell fluorescent staining was performed to analyze cell viability under different conditions. As shown in Fig. 7 A, the DC/TC percentage in the $BaTiO_3$/pTi + LIPUS group was statistically lower than that in the other three groups at 4 days. The DC/TC percentages in the pTi + LIPUS and $BaTiO_3$/pTi groups were lower than that in the pTi group. Meanwhile, the DC/TC percentage in the pTi + LIPUS group was statistically similar to that in the $BaTiO_3$/pTi group. At 7 days, the results were similar to those found at 4 day.

The typical proportion of apoptotic cells is shown in Fig. 7 B. Statistical analysis showed that differences in the apoptotic proportion followed the same trend as the differences in the DC/TC percentage across the four conditions. The proportion of apoptotic cells in the $BaTiO_3$/pTi + LIPUS group was statistically lower than that in the other three groups at 4 days. The proportion of apoptotic cells in the pTi + LIPUS and $BaTiO_3$/pTi groups was lower than that in the pTi group. Meanwhile, the proportion of apoptotic cells in the pTi + LIPUS group was statistically similar to that in the $BaTiO_3$/pTi group.

3.2.4. ALP activity and osteogenic gene marker analysis

Statistical analysis of intracellular ALP activity was performed after 7 and 14 days of incubation and is illustrated in Fig. 6C. ALP activity was significantly higher in the $BaTiO_3$/pTi + LIPUS, pTi + LIPUS, and $BaTiO_3$/pTi groups than in the pTi group at 7 days. Additionally, ALP activity was significantly higher in the $BaTiO_3$/pTi + LIPUS group than in the pTi + LIPUS and $BaTiO_3$/pTi groups. However, there was no statistical difference in ALP activity between the pTi + LIPUS and $BaTiO_3$/pTi groups. Furthermore, statistical analysis of the ALP activity in the four groups after 14 days showed similar results to those after 7 days, although ALP activity increased gradually with culture time.

The osteogenic differentiation-related genes ALP, OPN, OCN, RUNX2, and Col-1 were quantified using real-time quantitative PCR (RT-PCR) at 7 and 14 days. As Fig. 8 shows, the gene expression of COL-A1, ALP, OPN, and Runx2 at the mRNA level in the $BaTiO_3$/pTi + LIPUS group was significantly higher than that in the other three groups after 7 and 14 days. The ALP, COL-A1, and Runx2 gene expression was significantly higher in the pTi + LIPUS and $BaTiO_3$/pTi groups than in the pTi group at 7 and 14 days. There was no significant difference in the ALP, COL-A1, and Runx2 gene expression at 7 and 14 days between the pTi + LIPUS and $BaTiO_3$/pTi groups, while the OPN gene expression was significantly higher in the pTi + LIPUS and $BaTiO_3$/pTi groups than in the pTi group at 14 days.

3.3. In vivo testing

3.3.1. Micro-CT analysis

Representative 2D and 3D micro-CT images of implants in different groups at 6 and 12 weeks are shown in Fig. 9 A. After 6 weeks, the phenomenon of ingrowth of newly formed bone into the implants in the four groups was observed. The $BaTiO_3$/pTi + LIPUS group had more new bone tissue and thicker and coarser trabecular bone within the implants than the other three groups. Small patches of newly formed bone appeared in the $BaTiO_3$/pTi + LIPUS, pTi + LIPUS, and $BaTiO_3$/pTi groups, while newly formed bone sporadically appeared in the pTi group. At 12 weeks, all groups had more new bone tissue and thicker trabecular bone within the implants than at 6 weeks. A big flake of newly formed bone throughout the entire longitudinal axis of the implants was seen in the $BaTiO_3$/pTi + LIPUS group. There was also much newly formed bone tissue in the center of the implants. Newly formed bone was mainly found in the periphery of the implants in the pTi + LIPUS and $BaTiO_3$/pTi groups, although the phenomenon was similar to that seen in the $BaTiO_3$/pTi + LIPUS group. Large pieces of newly formed bone were rarely observed in the pTi group, and new bone tissue failed to run throughout the entire longitudinal axis of the implants. In addition, statistical analysis (Fig. 9C) showed that the BV/TV values were significantly higher in the $BaTiO_3$/pTi + LIPUS, pTi + LIPUS, and $BaTiO_3$/pTi groups than in the pTi group at 6 and 12 weeks. Meanwhile, the BV/TV values of the $BaTiO_3$/pTi + LIPUS group were statistically higher than those of the pTi + LIPUS and $BaTiO_3$/pTi groups at 6 and 12 weeks. However, there were no significant differences in the BV/TV values between the pTi + LIPUS and $BaTiO_3$/pTi groups at 6 and 12 weeks.

3.3.2. Fluorescence labeling analysis of newly formed bone

As shown in Fig. 9 B, several yellow lines (new bone labeled with tetracycline) and green lines (new bone labeled with calcein) were observed at the edge of the bone tissue. Additionally, the average width of the gaps between the yellow and green lines was calculated to find the MAR values. At 6 weeks, the MAR value of $BaTiO_3$/pTi + LIPUS was statistically higher than that of the other three groups (Fig. 9 D).

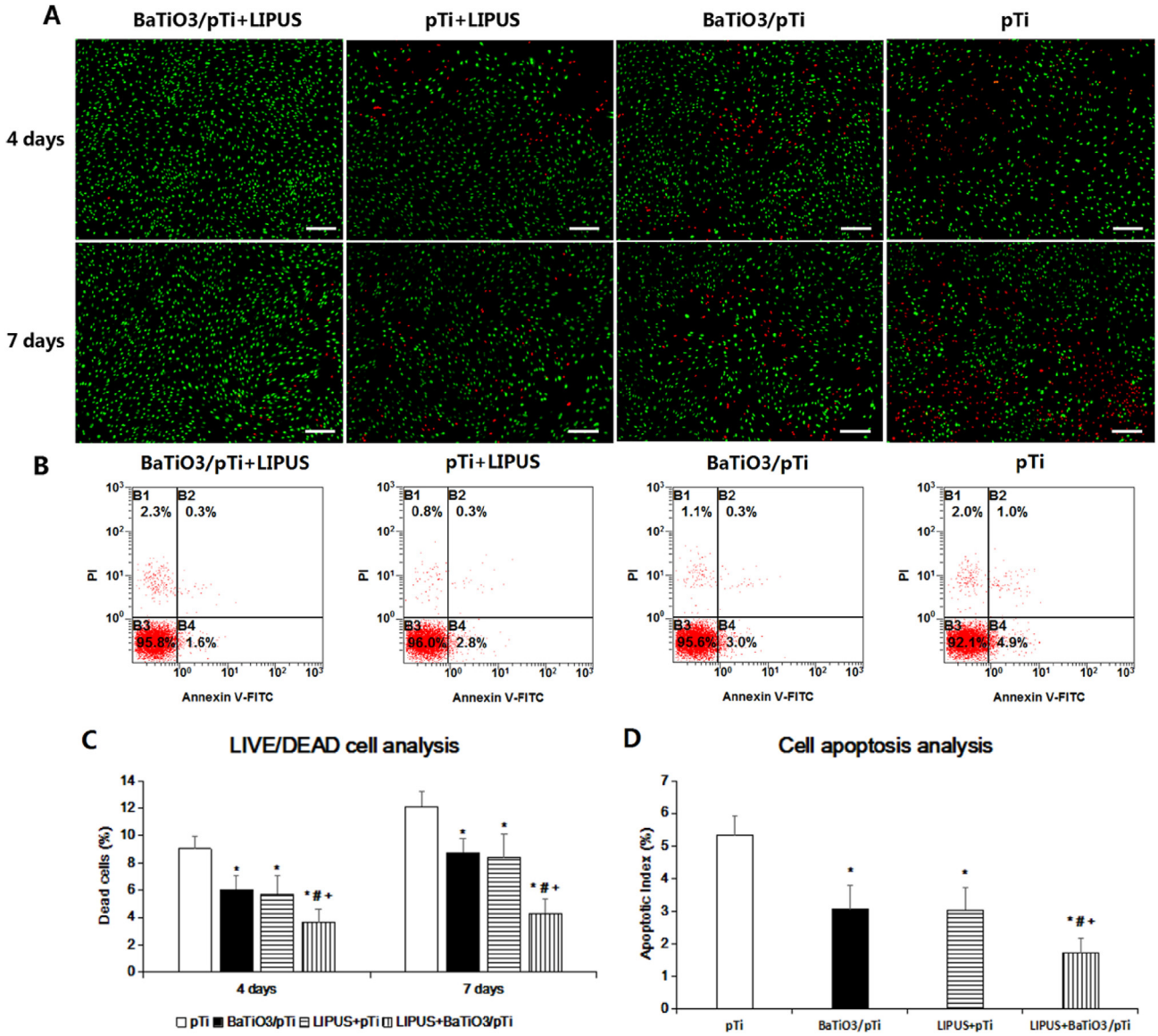

Fig. 7. (A)Fluorescent staining images of live/dead cells after incubation for 4 and 7 days in different groups. Scale bar: 200 μm. (B) Typical images of cell apoptosis detected with Annexin V-FITC/PI double-staining using flow cytometer. Statistical analysis of dead cells percentage (C) and apoptotic rate (D) in all the groups. *p < 0.05 vs. pTi, #p < 0.05 vs. $BaTiO_3$/pTi, +p < 0.05 vs. pTi + LIPUS.

The MAR values in the pTi + LIPUS and $BaTiO_3$/pTi groups were significantly higher than that in the pTi group. However, there was no statistical difference in the MAR values between the pTi + LIPUS and $BaTiO_3$/pTi groups. At 12 weeks, the change in the MAR values was similar to that seen at 6 weeks in all groups. The MAR values of the four groups at 12 weeks were lower than those at 6 weeks, but no significant differences were found.

3.3.3. Histological analysis

From the Van-Gieson staining (Fig. 10), we found that newly formed bone had begun to grow into the implants in all groups 6 weeks after implantation, but the trabecular bone was thin and irregular. Newly formed bone ran throughout the entire longitudinal axis of the implants in the $BaTiO_3$/pTi + LIPUS group, but there was less and more irregular trabecular bone in the other three groups. Moreover, newly formed bone only appeared at opposite ends of the long axis of implants in the pTi group, while newly formed bone was found in the center of the implants in the pTi + LIPUS and $BaTiO_3$/pTi groups. At 12 weeks, large pieces of new bone tissue were observed, and the trabecular bone was thicker and more neatly arranged in the four groups than at 6 weeks. New bone had almost filled the pores of the implants in the $BaTiO_3$/pTi + LIPUS group. Although large pieces of newly formed bone were found in the pTi + LIPUS and $BaTiO_3$/pTi groups, they barely ran throughout the long axis of the implants. Only small pieces of new bone tissue were found in the pTi group. Additionally, excellent integration was found between the newly formed bone and the implants in the $BaTiO_3$/pTi + LIPUS, pTi + LIPUS, and $BaTiO_3$/pTi groups at 12 weeks (Fig. 10 A3, B3, and C3). On the other hand, gaps between the newly formed bone and the implants were obviously seen in the pTi group (Fig. 10 D3). Furthermore, the percentages of newly formed bone in the $BaTiO_3$/pTi + LIPUS, pTi + LIPUS, and $BaTiO_3$/pTi groups were significantly higher than in the pTi group at 6 and 12 weeks. The percentages of the $BaTiO_3$/pTi + LIPUS group were statistically higher than those of the pTi + LIPUS and $BaTiO_3$/pTi groups at 6 and 12 weeks. However, there were no significant differences in the percentage of newly formed bone between the pTi + LIPUS and $BaTiO_3$/pTi groups at 6 and 12 weeks.

3.3.4. Biomechanical analysis

To evaluate the bonding strength of the bone and implants, the peak

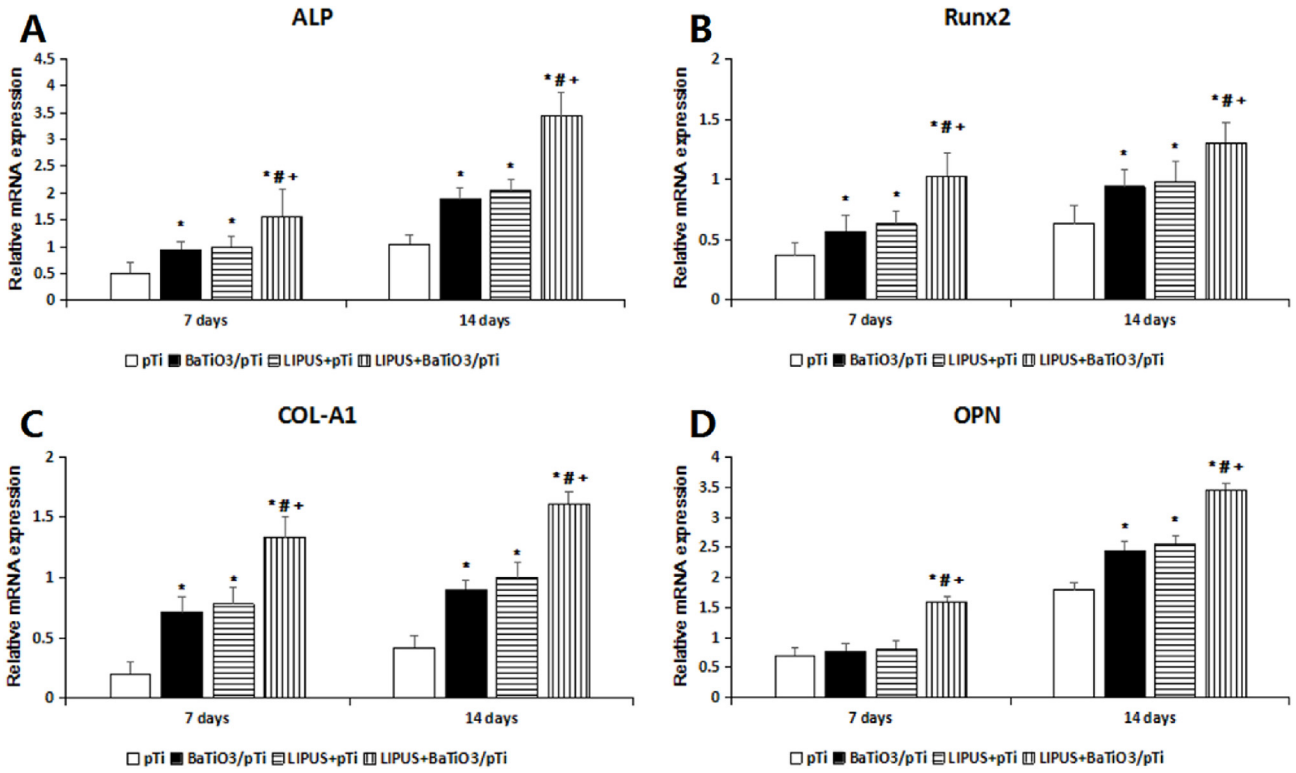

Fig. 8. Relative mRNA expression of ALP (A), Runx2 (B), COL-A1 (C) and OPN (D). *p < 0.05 vs. pTi, #p < 0.05 vs. $BaTiO_3$/pTi, +p < 0.05 vs. pTi + LIPUS.

pull-out load (N) of the implants was assessed 6 and 12 weeks after implantation (Fig. 11). At 6 weeks, the $BaTiO_3$/pTi + LIPUS, pTi + LIPUS, and $BaTiO_3$/pTi groups had significantly higher peak pull-out load in the loading modes of the tension test than the pTi group. It is worth noting that the $BaTiO_3$/pTi + LIPUS group achieved a more significant increase in peak pull-out load than the pTi + LIPUS and $BaTiO_3$/pTi groups. However, no significant difference was found between the pTi + LIPUS and $BaTiO_3$/pTi groups. By 12 weeks, peak pull-out loads of the three conditions ($BaTiO_3$/pTi + LIPUS, pTi + LIPUS, and $BaTiO_3$/pTi) had further increased compared with that of the pTi condition. Meanwhile, the trend in the differences in peak pull-out load among the four groups at 12 weeks was the same as that seen at 6 weeks. These data indicate that fusion between the bone tissue and the implant was most effective in the $BaTiO_3$/pTi + LIPUS group, which had the highest mechanical stability, and that the $BaTiO_3$/pTi + LIPUS group had the highest bonding strength between the bone and the implants among the four groups.

4. Discussion

At present, treatment methods for large segmental bone defects mainly involve bone grafting with a vascular pedicle [29], the Ilizarov technique [30,31], induced membrane technology [32], and other methods in clinical practice. With the application of the principles of healthcare engineering, a vital component of tissue engineering strategy is the scaffold, which serves as a template for interacting with surrounding tissue and providing structural support for the newly formed bone tissue [33]. The 3D structure of the scaffolds mimics the natural microenvironment and provides living space for cells, their porosity promotes recovery of blood supply and bone ingrowth, and their mechanical performance compensates for the insufficient support provided by the defect bone [34]. Nevertheless, ceramic scaffolds have the drawbacks of intrinsic brittleness, low resistance to crack propagation, and low bending strength which restrict the repair of challenging defects. With hierarchically-compositional and -structured pores close to the natural mineralized nano fibril counterparts, scaffolds based on electrospun polyester membranes are demonstrated with great potential for bone tissue engineering applications. Although polymer materials alone have already displayed some positive results for bone reparation, surface chemistry of these scaffolds that directly interact with the host cells is still the critical issue to be considered [35,36].

Nevertheless, they do not solve the problem of repairing large bone defects, which has puzzled orthopedic surgeons. Hence, an ideal treatment strategy for the defect should be selected, and it should involve certain elements, including a good scaffold as a support body, an adapted coating on the surface of the scaffold, and an additional auxiliary measure interacting with the scaffold or the coating. In this study, we fabricated porous Ti6Al4V scaffolds with a $BaTiO_3$ piezoelectric ceramic coating, which showed good hydrophilicity and high surface roughness. Moreover, the $BaTiO_3$ coating enhanced proliferation and osteogenic differentiation of BMSCs on the porous Ti6Al4V scaffolds in vitro and improved osteointegration and osteogenesis of the scaffolds in vivo, while the effect of LIPUS for porous Ti6Al4V scaffolds was similar to that of the $BaTiO_3$ coating. Additionally, the combination of the $BaTiO_3$ coating and LIPUS further strengthened their role. These results indicate that $BaTiO_3$ and LIPUS can enhance bone regeneration as independent factors and that they can also interact with each other to further promote new bone formation.

For bone ingrowth into the implant, sufficient pore size and pore interconnectivity in the scaffolds are necessary. To guarantee sufficient cellular viability in the interior of the implant, each pore should be connected with the others, and the size of the pores should be in the range of 400–1200 μm [37–39]. The porous Ti6Al4V scaffolds had fully interconnected pores and adjustable pore sizes (800 μm), and offered a satisfactory environment for new bone ingrowth. Meanwhile, to avoid stress shielding and adapt the scaffold stiffness to the surrounding bone tissue, 3D porous Ti6Al4V scaffolds were fabricated according to previous numerical analyses [40]. In terms of stress distribution, therefore, an adequate mechanical stimulus between the bone and implant contributes to the long-term stability of the implant.

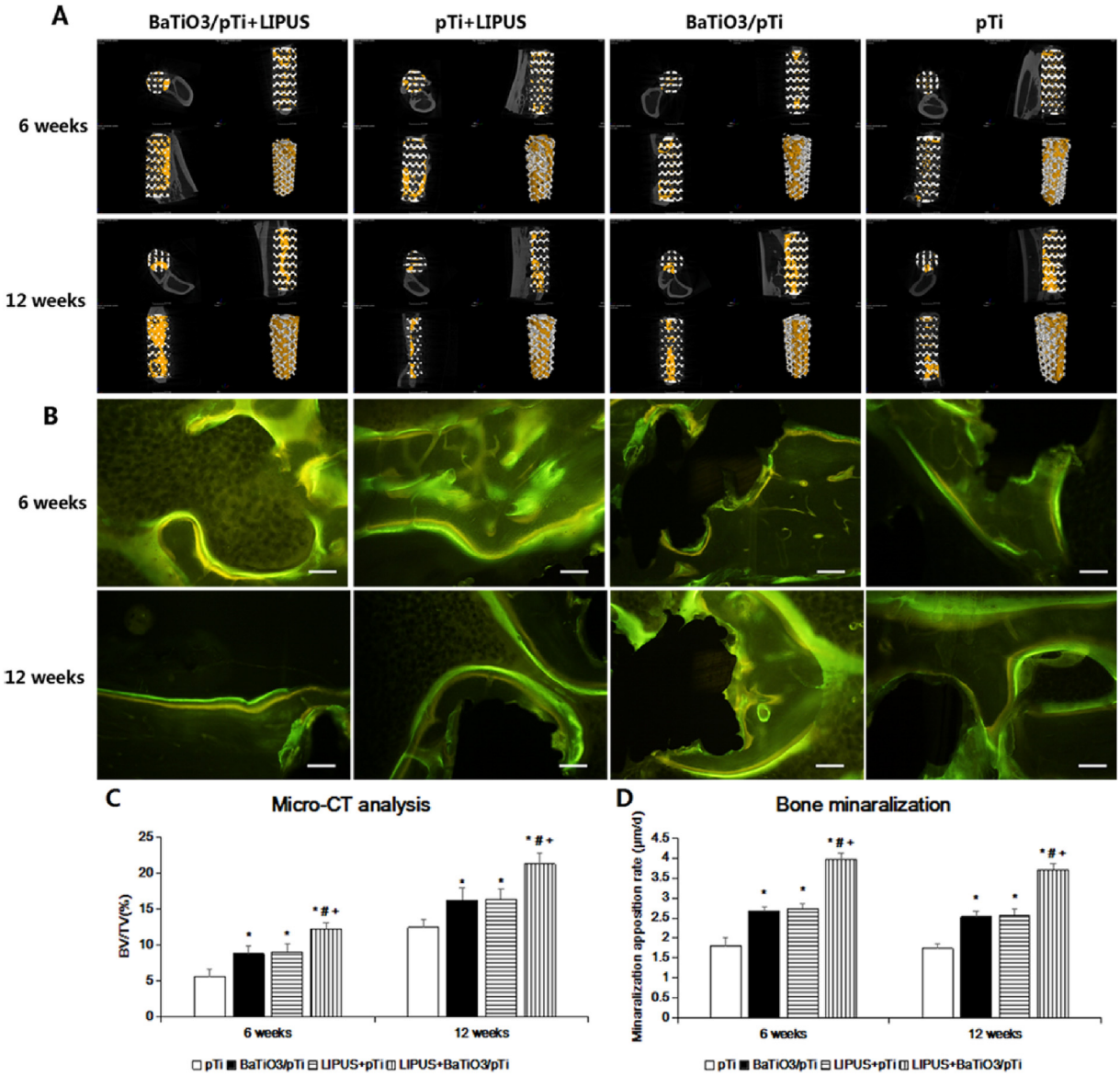

Fig. 9. (A) Micro-CT images of different groups at 6 and 12 weeks, and the yellow color component was newly formed bone in these scaffolds. The upper left of each small picture is a cross-sectional image through the center of the scaffold. The upper right is the image along the longitudinal axis of the scaffold through the center of the scaffold, parallel to the coronal plane of the rabbit. The lower left is the image along the longitudinal axis of scaffold, parallel to the sagittal plane of the rabbit. The upper right picture is a three-dimensional image of porous scaffold material. (B) Fluorescence labeling images of newly formed bone (yellow, tetracycline; green, calcein). Scale bar: 100 μm. (C) Percentages of regenerated bone volume/total volume (BV/TV) in these groups. (D) Statistical analysis of bone mineralization rate in all groups. *p < 0.05 vs. pTi, #p < 0.05 vs. $BaTiO_3$/pTi, +p < 0.05 vs. pTi + LIPUS.

Based on previous studies [41,42], the surface hydrophilicity and roughness of an implant affect the cell adhesion, proliferation, and differentiation on the scaffold. In the present study, $BaTiO_3$, as a piezoelectric ceramic, had higher hydrophilicity than metallic scaffolds (e.g., made of Ti, Ti6Al4V) and further enhanced the surface roughness of Ti6Al4V scaffolds. Li, Z. et al. proved that $BaTiO_3$ not only promoted cell proliferation but also improved the biological activity of the composite material [43]. Ciofani et al. fabricated water-soluble $BaTiO_3$ nanoparticles and found that they not only had good biocompatibility but also maintained a high dielectric constant and piezoelectric properties [44]. These results were the same as those observed in the present study. In addition, the effect of LIPUS on fractures and other healing responses has been studied in vitro [45–48], in animal models [49,50], and in clinical settings [51,52]. It is usually set to a 1.5 MHz sine wave with a pulse duration of 200 μs, a repeating pulse at 1 kHz, and an intensity of 30 mW/cm^2 in most studies [53] and represents very mild mechanical stimulation of the bone.

The CCK-8 assay showed that cell proliferation on the porous Ti6Al4V scaffolds was promoted by the $BaTiO_3$ coating and LIPUS (Fig. 5). Moreover, cells grown on the $BaTiO_3$/pTi + LIPUS scaffold stained more intensely with vinculin (Fig. 6) and had more lamellipodia extensions (Fig. 7) than those grown on pTi, $BaTiO_3$/pTi, or pTi + LIPUS scaffolds. Additionally, live/dead cell fluorescent staining and the cell apoptosis assay showed that the $BaTiO_3$ coating and LIPUS decreased cell death and increased cell activity and that the effect was further strengthened by the interaction of the two components. Apart from cell adhesion, proliferation, and apoptosis, cell differentiation is also critical for bone regeneration. The ALP activity of the cells was significantly increased by the $BaTiO_3$ coating and LIPUS, while the combination of a $BaTiO_3$ coating and LIPUS further increased the ALP activity. The mRNA levels of osteoblast-related genes (ALP, COL-A1, OPN, and Runx2) were measured by quantitative RT-PCR to assess the

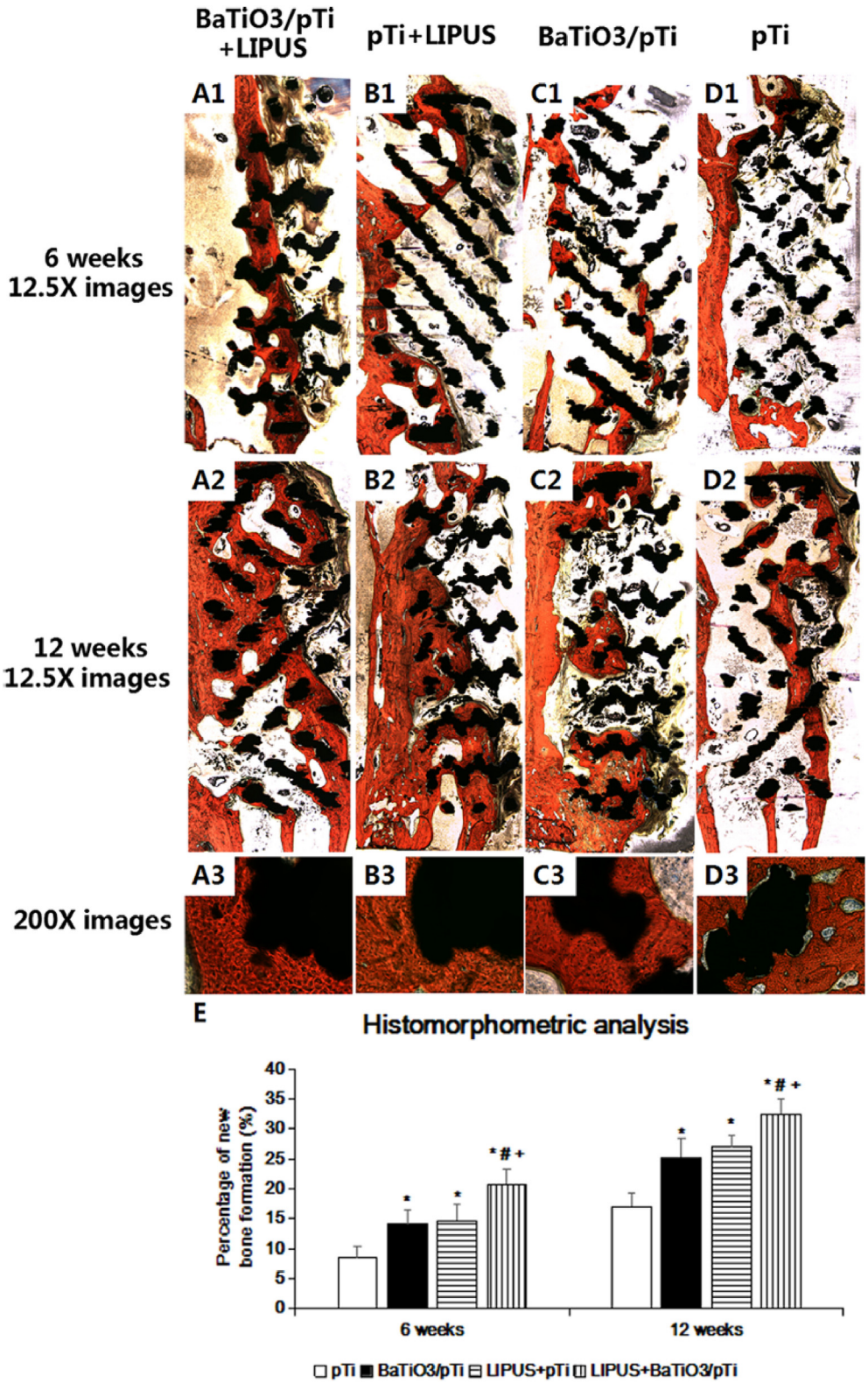

Fig. 10. (A、B、C and D)Van-Gieson staining of histological sections and (E) histomorphometric analysis of different groups at 6 and 12 weeks postoperation. The tissue stained with red color was the newly formed bone. The black referred to porous Ti6Al4V scaffold. *p < 0.05 vs. pTi, #p < 0.05 vs. $BaTiO_3$/pTi, +p < 0.05 vs. pTi + LIPUS.

differentiation state of the BMSCs. It was found that the gene expression of COL-A1, ALP, OPN, and Runx2 at the mRNA level in the $BaTiO_3$/pTi + LIPUS group was significantly higher than in the other three groups after 7 and 14 days. The ALP, COL-A1, and Runx2 gene expression was significantly higher in the pTi + LIPUS and $BaTiO_3$/pTi groups than in the pTi group at 7 and 14 days. There was no significant difference in the ALP, COL-A1, and Runx2 gene expression at 7 and 14 days between the pTi + LIPUS and $BaTiO_3$/pTi groups, while the OPN

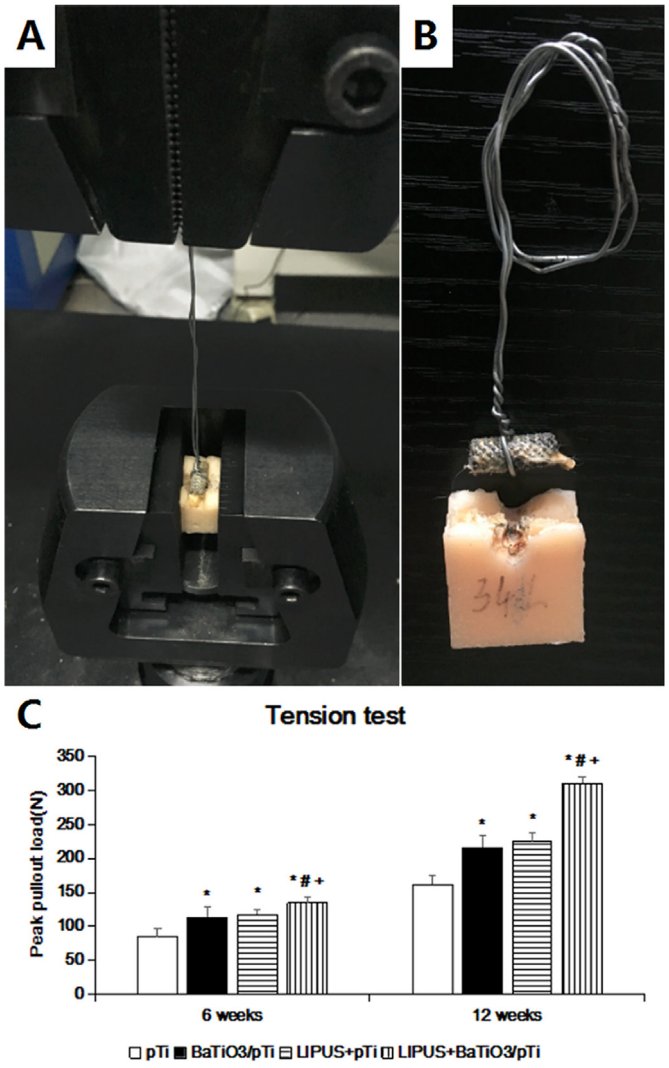

Fig. 11. (A) The sample was gripped by test device. (B) The sample after biomechanical test. (C) Statistical analysis of peak pullout land in all groups. *p < 0.05 vs. pTi, #p < 0.05 vs. $BaTiO_3$/pTi, +p < 0.05 vs. pTi + LIPUS.

gene expression was only significantly higher in the pTi + LIPUS and $BaTiO_3$/pTi groups than in the pTi group at 14 days. The gene expression of ALP, COL-A1, and Runx2 usually appears in the early stages of osteogenic differentiation of BMSCs, while OPN expression occurs late in the process of osteogenic differentiation. Therefore, the in vitro study indicated that the $BaTiO_3$ coating and LIPUS played an important role in cellular activities, including adhesion, proliferation, and differentiation, which is consistent with the results of previous studies [43,44,54]. It is worth noting that cellular activities were further enhanced by the combination of the two factors, which proved that the $BaTiO_3$ coating and LIPUS could interact with each other. That is, LIPUS could enhance the piezoelectric effect of $BaTiO_3$.

To investigate the treatment of large segmental bone defects, an appropriate animal model should be selected, because a good animal model can simulate the human situation in clinical practice and provide adequate results. In this study, a 13 mm segmental defect was created in the middle of the radius of New Zealand White rabbits to assess the capability for bone regeneration. We used micro-CT to calculate the amount of newly formed bone in the whole region of the implant to assess bone regeneration [5]. The $BaTiO_3$ coating and LIPUS induced bone regeneration on the Ti6Al4V scaffold at 6 and 12 weeks, while the combination of the $BaTiO_3$ coating and LIPUS led to a larger volume of regenerated bone. Additionally, the MAR results showed that the new bone formation rate of $BaTiO_3$/pTi + LIPUS was the highest among the four groups and demonstrated that $BaTiO_3$ and LIPUS as independent factors can promote bone regeneration and that they can interact with each other to stimulate new bone formation. Moreover, histological slices showed that large segmental bone defects had been completely repaired in the $BaTiO_3$/pTi + LIPUS group, because newly formed bone filled almost all of the pores of the implant. Meanwhile, no gap between the newly formed bone and the implant was observed in the $BaTiO_3$/pTi, pTi + LIPUS, and $BaTiO_3$/pTi + LIPUS groups. Furthermore, the biomechanical stability under tension at two different time points (6 and 12 weeks) was determined. We found that the $BaTiO_3$/pTi + LIPUS group had the highest tension, which indicated that there was more newly formed bone in the region of the implant. These results imply that $BaTiO_3$ and LIPUS not only promoted osteointegration and osteogenesis, respectively, but also further strengthened osteointegration and osteogenesis through their interaction with each other, which is consistent with our in vitro findings and previous studies [55,56].

The present study confirms that using the conditions in the $BaTiO_3$/pTi + LIPUS group is a promising method for bone regeneration of large segmental bone defects. The $BaTiO_3$ coating with a piezoelectric effect was easily fabricated on the surface of porous Ti6Al4V scaffolds, but the application of LIPUS is not convenient. Thus, in future work, first, a larger animal model, such as sheep, should be used to further verify the effectiveness of the $BaTiO_3$/pTi + LIPUS conditions to repair large bone defects. Additionally, the LIPUS device should be simplified for expedient use.

5. Conclusion

In the present study, a $BaTiO_3$ coating was successfully fabricated by a wet chemical method on the surface of porous Ti6Al4V scaffolds, which showed better surface hydrophilicity and roughness than pure porous Ti6Al4V scaffolds. In vitro studies, including the CCK-8 assay, live/dead cell staining, an apoptosis assay, immunofluorescent labeling, an ALP activity assay, and RT-PCR, suggested that the $BaTiO_3$ coating and LIPUS promoted adhesion, proliferation, and differentiation of BMSCs and that LIPUS activated the piezoelectric effect of the $BaTiO_3$ coating, further enhancing cell viability. In addition, the results of micro-CT, MAR, histological analysis, and biomechanical testing revealed that the $BaTiO_3$/pTi implants had greater osteointegration and osteogenesis properties with or without LIPUS in vivo than pTi implants. Especially with the combined conditions of $BaTiO_3$/pTi + LIPUS, large segmental bone defects were better repaired in this model than with the pTi, $BaTiO_3$/pTi, and pTi + LIPUS conditions. We concluded that the $BaTiO_3$ coating and LIPUS improved cell viability in vitro and increased new bone formation in vivo, that LIPUS activated the piezoelectric effect of the $BaTiO_3$ coating to further strengthen its role both in vitro and in vivo, and that pTi, the $BaTiO_3$ coating, and LIPUS were all necessary factors in the complete bone regeneration of a large segmental bone defect. Therefore, the $BaTiO_3$/pTi + LIPUS conditions showed promising potential as a method to repair long bone defects for clinical application.

CRediT authorship contribution statement

Bo Fan: Conceptualization, Methodology, Validation, Formal analysis, Investigation, Writing - original draft, Funding acquisition. **Zheng Guo:** Supervision, Project administration, Funding acquisition. **Xiaokang Li:** Writing - review & editing. **Songkai Li:** Methodology, Validation, Formal analysis. **Peng Gao:** Resources, Data curation, Validation. **Xin Xiao:** Investigation, Formal analysis. **Jie Wu:** Methodology, Validation. **Chao Shen:** Methodology, Formal analysis, Investigation, Visualization. **Yilai Jiao:** Resources, Methodology, Data curation. **Wentao Hou:** Resources, Visualization.

Declaration of competing interest

The authors declare that they have no conflict of interest.

Acknowledgments

This work was supported by grants from the National Key Research and Development Program of China (grant number 2017YFC1104901) to Zheng Guo, the National Natural Science Foundation of China (grant number 51771227) to Zheng Guo , the Youth Development Program of Chinese People's Liberation Army (No. 20QNPY069) to Bo Fan, the National Natural Science Foundation of China (No. 31800812) to Bo Fan, and the National Natural Science Foundation of China (grant number 51771227) to Zheng Guo.

References

[1] F. Lin, H. Sun, L. Yao, et al., Orthodontic treatment of severe anterior open bite and alveolar bone defect complicated by an ankylosed maxillary central incisor: a case report, Head Face Med. 10 (2014) 47.
[2] P. Megas, A. Saridis, A. Kouzelis, et al., The treatment of infected nonunion of the tibia following intramedullary nailing by the Ilizarov method, Injury 41 (2010) 294–299.
[3] B. Demiralp, T. Ege, O. Kose, et al., Reconstruction of intercalary bone defects following bone tumor resection with segmental bone transport using an Ilizarov circular externalfixator, J. Orthop. Sci. 19 (2014) 1004–1011.
[4] I.P. Schmitz, J.O. Hollinger, The critical size defect as an experimental model for cranium and ibulofacial nonunions, Clin. Orthop. Relat. Res. 205 (1986) 299–308.
[5] B. Fan, X. Wang, H. Zhang, et al., Improving the osteogenesis and degradability of biomimetic hybrid materials using a combination of bioglass and collagen I, Mater. Des. 112 (2016) 67–79.
[6] P. Gao, H. Zhang, Y. Liu, et al., Beta-tricalcium phosphate granules improve osteogenesis in vitro and establish innovative osteo-regenerators for bone tissue engineering in vivo, Sci. Rep. (2016), https://doi.org/10.1038/srep23367.
[7] J.A. Cobos, R.W. Lindsey, Z. Gugala, The cylindrical titanium mesh cage for treatment of a long bone segmental defect: description of a new technique and report of two cases, J. Orthop. Trauma 14 (2000) 54–59.
[8] N. Attias, R.W. Lindsey, Case reports: management of large segmental tibial defects using a cylindrical mesh cage, Clin. Orthop. Relat. Res. 450 (2006) 259–266.
[9] D.A. Heck, E.Y. Chao, F.H. Sim, et al., Titanium fibermetal segmental replacement prostheses: a radiographic analysis and review of current status, Clin. Orthop. Relat. Res. 204 (1986) 266–285.
[10] P.A. Ostermann, N. Haase, A. Rubberdt, et al., Management of a long segmental defect at the proximal meta-diaphyseal junction of the tibia using a cylindrical titanium mesh cage, J. Orthop. Trauma 16 (2002) 597–601.
[11] S.H. Wu, Y. Li, Y.Q. Zhang, et al., Porous titanium-6 aluminum-4 vanadium cage has better osseointegration and less micromotion than a poly-etherether-ketone cage in sheep vertebral fusion, Artif. Organs 37 (2013) E191 – 201.
[12] J. Parthasarathy, B. Starly, S. Raman, et al., Mechanical evaluation of porous titanium (Ti6Al4V) structures with electron beam melting (EBM), J. Mech. Behav. Biomed. Mater. 3 (2010) 249–259.
[13] C.M. Murphy, M.G. Haugh, F.J. O'Brien, The effect of mean pore size on cell attachment, proliferation and migration in collagenglycosaminoglycan scaffolds for bone tissue engineering, Biomaterials 31 (2010) 461–466.
[14] W. Xue, B.V. Krishna, A. Bandyopadhyay, et al., Processing and biocompatibility evaluation of laser processed porous titanium, Acta Biomater. 3 (2007) 1007–1018.
[15] Ting Zheng, Jiagang Wu, Dingquan Xiao, et al., Recent development in lead-free perovskite piezoelectric bulk materials, Prog. Mater. Sci. 98 (2018) 552–624.
[16] Chao Zhou, Wenfeng Liu, Dezhen Xue, et al., Triple-point-type morphotropic phase boundary based large piezoelectric Pb-free material—$Ba(Ti_{0.8}Hf_{0.2})O_3$-$(Ba_{0.7}Ca_{0.3})TiO_3$, Appl. Phys. Lett. 100 (2012) 222910.
[17] Chunlin Zhao, Haijun Wu, Fei Li, et al., Practical high piezoelectricity in barium titanate ceramics utilizing multiphase convergence with broad structural flexibility, J. Am. Chem. Soc. 140 (2018) 15252.
[18] I. Yasuda, Fundamental aspects of fracture treatment, J. Kyoto. Med. Soc. 4 (1953) 395.
[19] C.A.L. Bassett, O. RBecker, Generation of electric potential by bone in response to mechanical stress, Science 137 (1962) 1063.
[20] E. Lipiec, J. Kowalska, A. Wiechec, Infrared spectroscopy in molecular study of the piezoelectric effect in pig's shin bone, Acta Phys. Pol. 121 (2012) 539–542.
[21] Us Food and Drug Administration(FDA), Inc Exogen, Sonic accelrated fracture healing system(SAFHS), model 2 A: summary of safety and effectiveness. Premarket approval P900009, US Food and Drug Administration, Rockville, MD, October 5, 1994.
[22] Us Food and Drugs Administration(FDA), Exogen 2000, 3000, or sonic accelerated fracture healing system(SAFHS): summary of safety and effectiveness. Premarket approval P900009/supplement 6. Exogen, Inc, US Food and Drug Adminstration, Rockvile, MD, February 22, 2000.
[23] Y. Azuma, M. Ito, Y. Harada, et al., Low—intensity pulsed ultrasound accelerates rat femoral fracture heeling by acting on the various cellular reactions in the fracture callus, Bone Miner. Res. 16 (2001) 671–680.
[24] J. Parvizi, V. Parpura, J.F. Greenleaf, et al., Calcium signaling is required for ultrasound-stimulated aggrecan synthesis by rat chondmeytes, J. Orthop. Res. 20 (2002) 51–57.
[25] T. Kokubu, N. Matsui, H. Fujioka, et al., Low intensity pulsed ultrasound exposure increases prostaglandin E2 production via the induction of cyclooxygenase-2 mRNA in mouse osteoblasts, Biochem. Biophys. Res. Commun. 256 (1999) 284–287.
[26] T. Nishikori, M. Ochi, Y. Uchio, Effect of low-intensity pulsed ultrasound on proliferation and chondroitln sulfatesynthesis of cultured chondrocytes embedded in ateloedlagen gel, Biomed Mater Be 59 (2002) 201–206.
[27] P.A. Nolte, J.K. Klein-Nulend, G.H. Albers, et al., Low-intensity ultrasound stimulates endochondral ossification in vitro, J. Orthop. Res. 19 (2001) 301–307.
[28] I.J. Zhang, J. Huckle, C.A. Francomano, et al., The influence of pulsed low—-intensity ultrasound on matrix production of chondroeytes at different stages of differentiation: an explanation study, Ultrasound Med. Biol. 28 (2002) 1547–1553.
[29] R. Pollock, P. Stalley, K. Lee, Free vascularized fibula gratis in limb—salvage surgery, J. Reconstr. Microsurg. 21 (2005) 79–84.
[30] O. Karargyris, V.D. Polyzois, P. Karabinas, et al., Papineau debfidement,Ilizarov bone transport,and negative—pressure wound closure for septic bone defects of the tibia, Eur. J. Orthop. Surg. Traumatol. 24 (2014) 1013–1017.
[31] K. Wang, E. Edwards, Intramedullary skeletal kinetic distractor in the treatment of leg length discrepancy - a review of 16 cases and analysis of complications, J. Orthop. Trauma 26 (2012) e138–e144.
[32] A.C. Masquelet, F. Fitoussi, T. Begue, et al., Reconstruction of the long bones by the induced membrane and spongy autograft, Ann Chir Plast Esther 45 (2000) 346–353.
[33] Yanbo Zhang, Xiaochen Liu, Liangdan Zeng, et al., Polymer fiber scaffolds for bone and cartilage tissue engineering, Adv. Funct. Mater. 29 (36) (2019) 1903279.
[34] Tongtong Zhu, Yutao Cui, Mingran Zhang, et al., Engineered three-dimensional scaffolds for enhanced bone regeneration in osteonecrosis, Bioactive Materials 5 (3) (2020) 584–601.
[35] Jianxun Ding, Jin Zhang, Jiannan Li, et al., Electrospun polymer biomaterials, Prog. Polym. Sci. 90 (2019) 1–34.
[36] Xiangru Feng, Jiannan Li, Xi Zhang, et al., Electrospun polymer micro/nanofibers as pharmaceutical repositories for healthcare, J. Contr. Release 302 (2019) 19–41.
[37] A. Jonitz-Heincke, J. Wieding, C. Schulze, et al., Comparative analysis of the oxygen supply and viability of human osteoblasts in three dimensional titanium scaffolds produced by laser-beam or electron-beam melting, Mater 6 (2013) 5398–5409.
[38] J. Van der Stok, H. Wang, Y.S. Amin, et al., Enhanced bone regeneration of cortical segmental bone defects using porous titanium scaffolds incorporated with colloidal gelatin gels for time- and dose-controlled delivery of dual growth factors, Tissue Eng. 19 (2013) 2605–2614.
[39] P. Habibovic, M.C. Kruyt, M.V. Juhl, et al., Comparative in vivo study of six hydroxyapatite-based bone graft substitutes, J. Orthop. Res. 26 (2008) 1363–1370.
[40] Y. Li, W. Yang, X. Li, et al., Improving osteointegration and osteogenesis of three-dimensional porous Ti6Al4V scaffolds by polydopamine-assisted biomimetic hydroxyapatite coating, ACS Appl. Mater. Interfaces 7 (2015) 5715–5724.
[41] C. Bayram, M. Demirbilek, N. Caliskan, et al., Osteoblast activity on anodized titania nanotubes: effect of simulated body fluid soaking time, J. Biomed. Nanotechnol. 8 (2012) 482–490.
[42] D.O. Costa, P.D. Prowse, T. Chrones, et al., The differential regulation of osteoblast and osteoclast activity by surface topography of hydroxyapatite coatings, Biomaterials 34 (2013) 7215–7226.
[43] Z. Li, Y. Qu, X. Zhang, et al., Bioactive nano-titania ceramics with biomechanical compatibility prepared by doping with piezoelectric $BaTiO_3$, Acta Biomater. 5 (2009) 2189–2195.
[44] G. Ciofani, S. Danti, S. Moscato, et al., Preparation of stable dispersion of barium titanate nanoparticles: potential applications in biomedicine, Colloids Surf. B Biointerfaces 76 (2010) 535–543.
[45] A. Suzuki, T. Takayama, N. Suzuki, et al., Daily low-intensity pulsed ultrasound stimulates production of bone morphogenetic protein in ROS 17/2.8 cells, J. Oral Sci. 51 (2009) 29–36.
[46] A. Suzuki, T. Takayama, N. Suzuki, et al., Daily low-intensity pulsed ultrasound-mediated osteogenic differentiation in rat osteoblasts, Acta Biochim. Biophys. Sin. 41 (2009) 108–115.
[47] T. Takayama, N. Suzuki, K. Ikeda, et al., Low-intensity pulsed ultrasound stimulates osteogenic differentiation in ROS 17/2.8 cells, Life Sci. 80 (2007) 965–971.
[48] K. Ikeda, T. Takayama, N. Suzuki, et al., Effects of low-intensity pulsed ultrasound on the differentiation of C2C12 cells, Life Sci. 79 (2006) 1936–1943.
[49] Y. Azuma, M. Ito, Y. Harada, et al., Low-intensity pulsed ultrasound accelerates rat femoral fracture healing by acting on the various cellular reactions in the fracture callus, J. Bone Miner. Res. 16 (2001) 671–680.
[50] S.J. Wang, D.G. Lewallen, M.E. Bolander, et al., Low intensity ultrasound treatment increases strength in a rat femoral fracture model, J. Orthop. Res. 12 (1994) 40–47.
[51] P.H. Lubbert, R.H. van der Rijt, L.E. Hoorntje, et al., Low-intensity pulsed ultrasound (LIPUS) in fresh clavicle fractures: a multi-centre double blind randomised controlled trial, Injury 39 (2008) 1444–1452.
[52] T.K. Kristiansen, J.P. Ryaby, J. McCabe, et al., Accelerated healing of distal radial fractures with the use of specific, low-intensity ultrasound: a multicenter, prospective, randomized, double-blind, placebo-controlled study, J Bone Joint Surg Am 79 (1997) 961–973.
[53] S.L. Ferreri, R. Talish, T. Trandafir, et al., Mitigation of bone loss with ultrasound induced dynamic mechanical signals in an OVX induced rat model of osteopenia, Bone 48 (2011) 1095–1102.
[54] S.R. Angle, K. Sena, D.R. Sumner, et al., Osteogenic differentiation of rat bone marrow stromal cells by various intensities of low-intensity pulsed ultrasound, Ultrasonics 51 (2011) 281–288.
[55] J. Feng, H. Yuan, X. Zhang, Promotion of osteogenesis by a piezoelectric biological ceramic, Biomaterials 18 (1997) 1531–1534.
[56] S. Rutten, P.A. Nolte, C.M. Korstjens, et al., Low-intensity pulsed ultrasound increases bone volume, osteoid thickness and mineral apposition rate in the area of fracture healing in patients with a delayed union of the osteotomizedfibula, Bone 43 (2008) 348–354.